

Deformable registration of diffusion tensor MR images with explicit orientation optimization

Hui Zhang ^{a,*}, Paul A. Yushkevich ^a, Daniel C. Alexander ^b, James C. Gee ^a

^a Penn Image Computing and Science Laboratory (PICSL), Department of Radiology, University of Pennsylvania, 3600 Market Street, Suite 370, Philadelphia, PA 19104, USA

^b Department of Computer Science, University College London, Gower Street, London WC1E 6BT, UK

Received 23 January 2006; received in revised form 8 May 2006; accepted 8 June 2006

Available online 8 August 2006

Abstract

In this paper, we present a novel deformable registration algorithm for diffusion tensor MR images that enables explicit optimization of tensor reorientation. The optimization seeks a piecewise affine transformation that divides the image domain into uniform regions and transform each region affinely. The objective function captures both the image similarity and the smoothness of the transformation across region boundaries. The image similarity enables explicit orientation optimization by incorporating tensor reorientation, which is necessary for warping diffusion tensor images. The objective function is formulated in a way that allows explicit implementation of analytic derivatives to drive fast and accurate optimization using the conjugate gradient method. By explicitly optimizing tensor reorientation, the algorithm is designed to take advantage of similarity measures comparing tensors as a whole. The optimal transformation is hierarchically refined in a subdivision framework. A comparison with affine registration for inter-subject normalization of 8 subjects shows that the proposed algorithm improves the alignment of several major white matter structures examined: the anterior thalamic radiations, the inferior fronto-occipital fasciculi, the corticospinal/corticobulbar tracts and the genu and the splenium of the corpus callosum. The alignment of white matter structures is assessed using a novel scheme of computing distances between the corresponding fiber bundles derived from tractography.

© 2006 Elsevier B.V. All rights reserved.

Keywords: Diffusion tensor MRI; Registration; Spatial normalization; Tractography

1. Introduction

Diffusion tensor magnetic resonance imaging (DT-MRI) (Basser et al., 1994) is a water diffusion imaging technique used to provide unique insight into the white matter organization in human brains (Jones et al., 1999; Wakana et al., 2004). Water diffusion can reveal certain microscopic structure of the underlying tissue, particularly the presence of fibrous structures. For instance, in white matter, which consists of packed axon fibers, diffusion is anisotropic due to restricted movement of water molecules perpendicular to the axon fibers; the direction along which water dif-

fuses most freely coincides with the orientation of the fibers. Diffusion tensor images contain at each voxel a symmetric 2nd-order Cartesian tensor that allows us to measure both the water diffusion anisotropy and the preferred diffusion orientation. This unique ability to reveal the orientation of fiber bundles makes diffusion tensor images an ideal choice for understanding and analyzing white matter structures.

Spatial normalization of groups of diffusion tensor images acquired from different subjects enables accurate mapping of characteristics of the diffusion tensor, such as diffusion anisotropy and orientation, within these images. It has important applications in assisting clinical studies into the variation of measurements derived from the diffusion tensor over normal and patient population groups (see Park et al. (2004) for an example). Image registration of

* Corresponding author. Tel.: +1 215 662 3651; fax: +1 215 615 3681.
E-mail address: huiz@cis.upenn.edu (H. Zhang).

diffusion tensor images plays a key role in realizing spatial normalization. Compared to registering scalar images, the registration of diffusion tensor images is particularly challenging not only due to the multi-dimensionality of the data, but also because one must ensure that the tensor orientations remain consistent with the anatomy after image transformations (Alexander et al., 2001). Earlier diffusion tensor image registration techniques circumvent tensor reorientation by registering scalar images derived from diffusion tensor images (Jones et al., 2002; Guimond et al., 2002), thus discarding the orientation component of the data. Some other methods register actual tensor images but not reorienting the tensors during registration (Alexander and Gee, 2000; Ruiz-Alzola et al., 2002), thus introducing inaccuracies in image matching. Later Park et al. (2003) showed that using diffusion tensors as a whole improved the quality of registration by better matching the diffusion tensors orientation information; but their method only applied tensor reorientation iteratively and tensor reorientation was not explicitly optimized. Curran and Alexander (2003) then demonstrated that explicitly optimizing tensor reorientation during affine registration of synthetic images improved image matching. However their method (Curran and Alexander, 2004) is not derivative-based and their registration optimization tends to have difficulties with local minima. We proposed an affine registration algorithm that both explicitly optimizes tensor reorientation and has a novel derivative-based formulation in Zhang et al. (2004). Our synthetic examples show that our derivative-based method is faster and reaches global minima more consistently than the method not using derivatives. Most recently, Cao et al. (2005) developed a large deformation diffeomorphic registration algorithm for vector fields. The algorithm was applied to register diffusion tensor images by matching their corresponding principal eigenvectors. A more complete review of the literature can be found in Gee and Alexander (2005).

In this paper, we describe a novel algorithm for deformable registration of diffusion tensor images that incorporates explicit optimization of tensor reorientation in an analytic manner. The optimization seeks an optimal deformation from the family of piecewise affine transformations that divide the image domain into uniform regions and transform each region affinely. The objective function has terms sensitive to both the image similarity and the smoothness of the transformation across contiguous regions. The objective function has analytic derivatives and we use the conjugate gradient method for fast and accurate optimization. By explicitly optimizing tensor reorientation, the algorithm is designed to take advantage of similarity measures comparing tensors as a whole. In a subdivision framework, we hierarchically refine the optimal piecewise affine transformation. The proposed algorithm was applied to inter-subject registration. The results were evaluated using a novel scheme for assessing the alignment of anatomically corresponding white matter structures. We showed that our deformable algorithm improved the align-

ment of a number of white matter structures examined compared to affine registration. The statistical properties of the registered images as a whole were also analyzed and the result is consistent with the one from evaluating white matter alignment of the individual image.

In Section 2, we will review the properties of diffusion tensor images and the general issues of diffusion tensor image registration. Our method is then presented in Section 3. The details of its evaluation are discussed next in Section 6, followed by the results of the evaluation in Section 5. In Section 6, we discuss the implication of our results, and future directions to take to address the limitations of this work. We conclude with a summary of the contributions in Section 7.

2. Background

2.1. Diffusion tensor MRI

Diffusion tensor MRI characterizes the water diffusion by measuring the apparent diffusion tensor in each voxel of an MRI volume. The method assumes that water molecules move according to a simple anisotropic diffusion process so that the displacement \mathbf{x} of a water molecule over a fixed time t is modeled as a random variable that follows the multivariate normal distribution p with the mean at the origin and covariance $2t\mathbf{D}$, where \mathbf{D} is the diffusion tensor, a symmetric and positive-definite (SPD) 3-by-3 matrix.

Diffusion-weighted MRI sensitizes the MRI measurement to diffusion by introducing diffusion-weighting gradient-pulses to standard sequences. The diffusion-sensitized sequence allows the sampling of the apparent diffusion coefficients (ADC) along the directions of the gradient-pulses. Hereafter, we will use the term “ADC profile” to refer to the ADCs as a function of spatial direction. Because \mathbf{D} has six independent components, measurements from a minimum of six independent directions have to be acquired. The apparent diffusion tensor \mathbf{D} is the best fit tensor to the sampled ADC profile using the Gaussian diffusion model. Under the Gaussian diffusion model, the ADC profile, $d_{\mathbf{D}}(\hat{k})$, and the diffusion tensor, \mathbf{D} , are related by the equation

$$d_{\mathbf{D}}(\hat{k}) = \hat{k}^T \mathbf{D} \hat{k}, \quad (1)$$

where \hat{k} is a unit vector.

The diffusion tensor provides estimates of the *mean diffusivity*, *anisotropy* and *dominant orientation* of diffusion. The eigenvalues $\lambda_1 \geq \lambda_2 \geq \lambda_3$ and corresponding eigenvectors $\{\mathbf{e}_i\}_{i=1,2,3}$ of \mathbf{D} are convenient for establishing these estimates. The mean diffusivity, the ADCs averaged over all the spatial directions, is proportional to the mean squared displacement of water molecules which indicates the mobility of water molecules. The mean diffusivity is equal to one third of the trace of the diffusion tensor $\text{Tr}(\mathbf{D}) = \sum_{i=1}^3 \lambda_i$. Fig. 1(b) maps $\text{Tr}(\mathbf{D})$ over an axial slice through a healthy human brain with the corresponding slice through the T1-weighted volume of the same individual shown in Fig. 1(a).

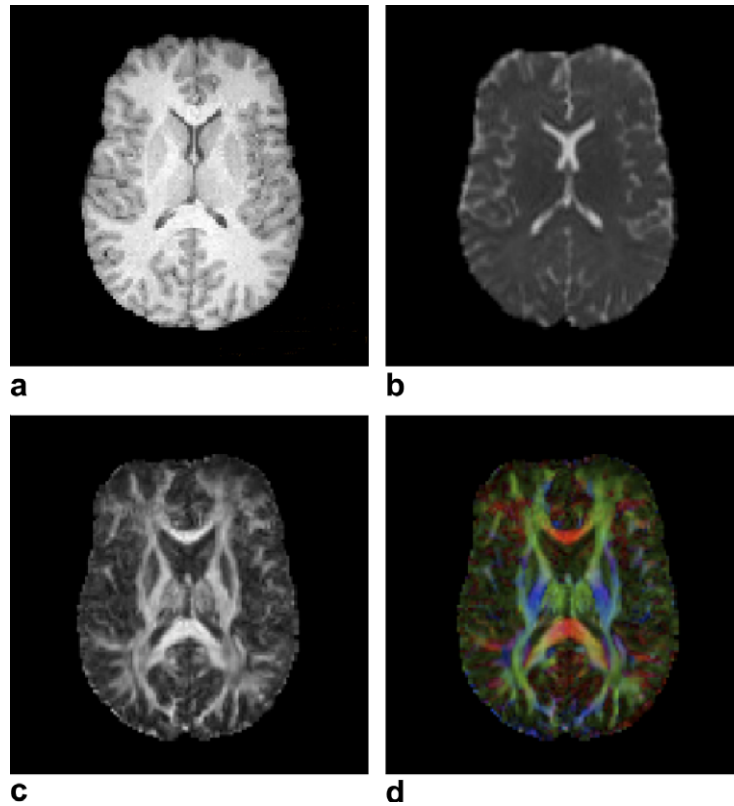


Fig. 1. The axial slice 24 of the diffusion tensor image chosen as the template in this study. The T1-weighted image, the trace, the FA and the color-coded principal eigenvector maps are shown in the panels (a), (b), (c) and (d) respectively. In (d), the directions encoded by each color channel are mediolateral (left to right) for red, anteroposterior (front to back) for green and superoinferior (top to bottom) for blue. (For interpretation of the references to colour in this figure legend, the reader is referred to the Web version of this article.)

The values of $\text{Tr}(\mathbf{D})$ are the highest in cerebral spinal fluid, e.g., in the ventricles, where the water diffuses most freely. The anisotropy of diffusion can be derived from the shape of the distribution p . The Gaussian distribution has ellipsoidal contours and the relative lengths of the major axes of the ellipsoids are proportional to the square roots of the eigenvalues. The differences in the eigenvalues reflect the anisotropy. A commonly used measure is the fractional anisotropy (FA)

$$v = \sqrt{\frac{3 \sum_{i=1}^3 (\lambda_i - \frac{1}{3} \text{Tr}(\mathbf{D}))^2}{\sum_{i=1}^3 \lambda_i^2}}, \quad (2)$$

which is the normalized standard deviation of the eigenvalues. The values of v vary from 0 to 1 with the higher values corresponding to greater diffusion anisotropy. Fig. 1(c) shows the FA map of the same slice as in Fig. 1(b). The higher values of v are found in the white matter regions which contain densely packed fiber bundles that cause anisotropic diffusion by restricting water movement along directions perpendicular to the fiber bundles. In the regions where the underlying fiber bundles have similar orientation, water molecules move preferentially along the orien-

tation of the fiber bundles. The distribution p thus has prolate (cigar-shaped) ellipsoidal contours and \mathbf{D} has the eigenvalues $\lambda_1 \gg \lambda_2 \approx \lambda_3$. The eigenvector \mathbf{e}_1 , the principal eigenvector, provides an estimate of the fiber direction. To visualize fiber orientations, a popular method (Pajevic and Pierpaoli, 1999) is to use RGB vectors proportional to the fractional anisotropy weighted principal eigenvectors. Fig. 1(d) shows such a color map corresponding to the same slice as in Fig. 1(b). The orientation of the fiber bundles underlying the white matter that appears homogeneous in the T1-weighted image (Fig. 1(a)) is revealed in details, demonstrating the power of DT-MRI.

DT-MRI has its limitations however. In particular, around the regions where two fiber bundles cross, the distribution p has the oblate (pancake-shaped) ellipsoidal contours with the eigenvalues $\lambda_1 \approx \lambda_2 \gg \lambda_3$. Dominant fiber orientations in this case can not be discerned without using more general models of molecular displacement (see Alexander (2005) for a survey).

2.2. Registration of diffusion tensor images

Using diffusion tensor data, registration routines that are capable of matching orientation promise to align white matter in a manner that is consistent with its inherent orga-

nization. Registration of these images presents several unique challenges which we will discuss below while formally formulating the registration problem.

Similar to any other registration task (Maintz and Viergever, 1998), diffusion tensor image registration can be formulated as an optimization problem of finding an optimal transformation \mathbf{v} within some image transformation space \mathbf{V} , such that, for two input images, \mathbf{I}_t (the template) and \mathbf{I}_s (the subject), a measure of similarity $\phi(\mathbf{I}'_t, \mathbf{I}_s)$ is optimized, with \mathbf{I}'_t being the image warped from \mathbf{I}_t by \mathbf{v} . For scalar-valued images, image transformations merely change the location of each point \mathbf{x} , i.e., $\mathbf{I}'_t(\mathbf{v}(\mathbf{x})) = \mathbf{I}_t(\mathbf{x})$. Image warping is less simple for diffusion tensor images. Transformations of diffusion tensor images also change the orientation of diffusion tensors (Alexander et al., 2001), i.e., the relation between the template \mathbf{I}_t and the warped template \mathbf{I}'_t is instead

$$\mathbf{I}'_t(\mathbf{v}(\mathbf{x})) = R[\mathbf{I}_t(\mathbf{x})],$$

where R denotes some operator that accounts for the change in orientation of diffusion tensors induced by the transformation \mathbf{v} . The reorientation operator R needs to ensure that the orientation of diffusion tensors remains consistent with the anatomy after an image transformation. This is illustrated in Fig. 2. Fig. 2(a) shows schematically an anisotropic region in a diffusion tensor image. Figs. 2(b) and (c) show the same slice after a 30° rotation about z-axis without and with tensor reorientation. Observe that after applying reorientation (rotating each tensor by 30°), the original pattern of tensor orientation is recovered from the one that is disrupted in Fig. 2(b).

Finding suitable similarity measures for diffusion tensors is the second challenge for diffusion tensor image registration. A numerical estimate of the image similarity ϕ is typically computed by comparing the data values at corresponding points in the two images, \mathbf{I}_t and \mathbf{I}_s . In the case of diffusion tensor images, a comparative measure of similarity between diffusion tensors is required. To fully exploit the information in diffusion tensor images, we need similarity measures that are sensitive to all aspects of the diffusion tensor including size, shape and, most importantly, orientation. Assuming $\delta(\cdot, \cdot)$ denotes such a similarity measure

between diffusion tensors, the image similarity is the sum of squares of the similarities of the diffusion tensors in corresponding voxels:

$$\begin{aligned} \phi(\mathbf{I}_t, \mathbf{I}_s, \mathbf{v}) &= \int_{\Omega} \delta^2(\mathbf{I}'_t(\mathbf{v}(\mathbf{x})), \mathbf{I}_s(\mathbf{v}(\mathbf{x}))) d\mathbf{x} \\ &= \int_{\Omega} \delta^2(R[\mathbf{I}_t(\mathbf{x})], \mathbf{I}_s(\mathbf{v}(\mathbf{x}))) d\mathbf{x}. \end{aligned} \quad (3)$$

This is illustrated in Fig. 3.

To model image differences that arise from complex development or anatomical variability, deformable registration that employs transformation models of high degrees of freedom is required (Lester and Arridge, 1999). However, because the similarity functional ϕ becomes fundamentally under-constrained, a regularization functional $\psi(\mathbf{v})$ is generally introduced to address the ill-posedness of the problem. The optimization problem becomes

$$\arg \min_{\mathbf{v} \in \mathbf{V}} (\phi(\mathbf{I}_t, \mathbf{I}_s, \mathbf{v}) + \psi(\mathbf{v})), \quad (4)$$

which, in general, is highly non-linear. The high degrees of freedom of the transformation model results in a solution space of large dimension. Non-linear optimization of this kind can be solved both faster and more accurately when the objective function has analytic derivatives that we can implement explicitly to guide the optimization (Press et al., 1993).

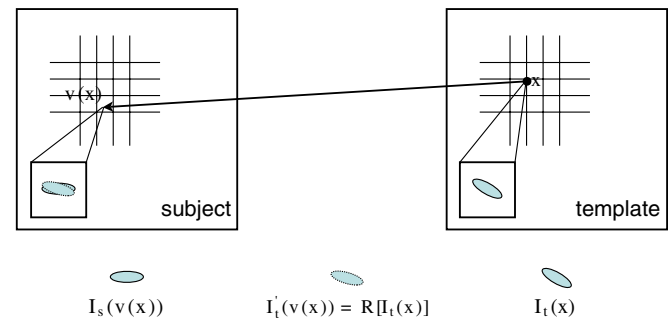


Fig. 3. A 2D illustration of the derivation of the image similarity for two diffusion tensor images.

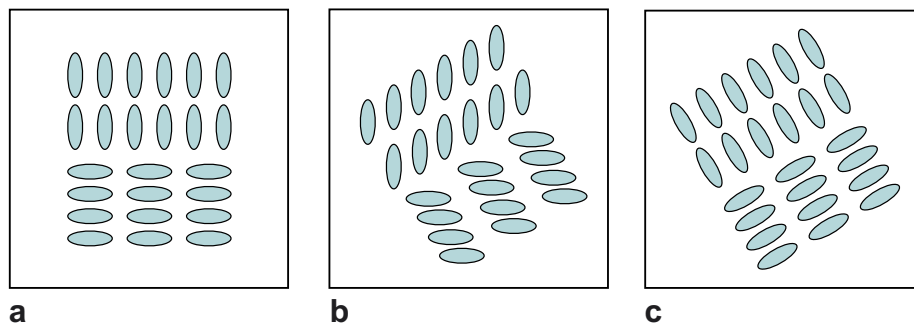


Fig. 2. Diffusion tensor reorientation. Panel (a) shows schematically an axial slice in an anisotropic region of a diffusion tensor image. Panel (b) shows the same slice after a 30° rotation about the z-axis with no reorientation of the diffusion tensors. Panel (c) shows the slice after the same rotation, but with each tensor transformed by the same rotation.

3. Method

Our deformable registration algorithm for diffusion tensor images enables explicit optimization of tensor reorientation. Explicit optimization of tensor reorientation allows us to take advantage of similarity measures comparing full tensors. Our objective function has analytic derivatives which enables faster and more accurate optimization. In the following, we begin by reviewing the known diffusion tensor similarity measures with an emphasis on the ones comparing full tensors that can benefit from our algorithm. Then we review the tensor reorientation formulation essential for understanding our algorithm. Next we present the core affine registration formulation that enables explicit analytic tensor reorientation optimization. Finally we discuss the incorporation of the smoothness term for regularizing the solution.

3.1. Similarity measures of diffusion tensors

Different measures for comparing diffusion tensors have been proposed in the literature (Alexander and Gee, 2000). The most simple ones compare transformation-invariant scalar quantities such as $\text{Tr}(\mathbf{D})$ or fractional anisotropy v . Although such scalar values permit the use of traditional intensity-based registration methods, they ignore the rich orientation information encoded in diffusion tensors. An alternative is to base a similarity measure on the comparison of all tensor elements. Mathematically we can construct such similarity measures by equipping the vector space of tensors with an inner product $\langle \cdot, \cdot \rangle$. The induced norm $\|\cdot\|$ of the resulting metric space is then a natural choice for measuring tensor similarities. The most commonly used diffusion tensor similarity measure is the Euclidean distance between two tensors defined as $\|\mathbf{D}_1 - \mathbf{D}_2\|_C = \sqrt{\text{Tr}((\mathbf{D}_1 - \mathbf{D}_2)^2)}$, induced by the Cartesian tensor inner product $\langle \mathbf{D}_1, \mathbf{D}_2 \rangle_C = \text{Tr}(\mathbf{D}_1 \mathbf{D}_2)$.

In Zhang et al. (2004), we proposed a novel inner product that induces a similarity measure that is based on comparing ADC profiles. Since diffusion tensors are summaries of the ADC profiles within the voxels under consideration, we expect that a metric formulated using ADC profiles to perform as well or better than full tensor metrics. By comparing ADC profiles directly, our proposed measure can be applied both to diffusion tensors and to higher-order models of diffusion. An ADC profile is formally defined as $d(\hat{k}) : \mathbb{S}^2 \rightarrow \mathbb{R}^+$, a positive function defined over the unit sphere \mathbb{S}^2 . Under the Gaussian model of diffusion, an ADC profile can be uniquely defined by a diffusion tensor as in Eq. (1). In contrast, under the general model, ADC profiles are functions that form an open subset of the space of complex-valued L^2 spherical functions, which themselves form an infinite-dimensional Hilbert space, when associated with the inner product

$$\langle f, g \rangle = \int_{\mathbb{S}^2} f(\hat{k}) g^*(\hat{k}) d\hat{k}, \quad (5)$$

where $g^*(\hat{k})$ is the complex conjugate of $g(\hat{k})$. The induced L^2 norm is simply $\|f\| = \sqrt{\langle f, f \rangle}$, allowing us to define the distance metric between two ADC profiles as $\|f - g\|$.

A natural way to compute the inner product (5) is to express the spherical functions in terms of spherical harmonics, $Y_l^m(\theta, \phi)$,

$$f(\theta, \phi) = \sum_{l=0}^{\infty} \sum_{m=-2l}^{2l} F_{2l}^m Y_{2l}^m(\theta, \phi),$$

where the unit vector \hat{k} is parameterized by the polar coordinate θ and the azimuthal coordinate ϕ . Because ADC profiles have zero imaginary components, $F_{2l}^{-m} = (-1)^m (F_{2l}^m)^*$; and because of the antipodal symmetry, the harmonic expansion has only even terms in the first index. The scheme for reconstructing the coefficients F_{2l}^m to model general ADC profiles can be found in Alexander et al. (2002). Given these coefficients and the orthogonality among spherical harmonics, the inner product can be computed using

$$\langle f, g \rangle = \sum_{l=0}^{\infty} \sum_{m=-2l}^{2l} F_{2l}^m (G_{2l}^m)^*. \quad (6)$$

Under the Gaussian model of diffusion, the ADC profile can be decomposed into spherical harmonics by algebraic manipulation, and the series has exactly six non-zero coefficients:

$$\begin{aligned} F_0^0 &= \frac{\sqrt{4\pi}}{3} (D_{11} + D_{22} + D_{33}), \\ F_2^0 &= \frac{1}{3} \sqrt{\frac{4\pi}{5}} (-D_{11} - D_{22} + 2D_{33}), \\ F_2^1 &= -(F_2^{-1})^* = \sqrt{\frac{2\pi}{15}} (-2D_{13} + 2iD_{23}), \\ F_2^2 &= (F_2^{-2})^* = \sqrt{\frac{2\pi}{15}} (D_{11} - D_{22} - 2iD_{12}), \end{aligned}$$

and the L^2 inner product (6) can be expressed algebraically in terms of the diffusion tensors

$$\langle \mathbf{D}_1, \mathbf{D}_2 \rangle_L = \frac{8\pi}{15} \left(\langle \mathbf{D}_1, \mathbf{D}_2 \rangle_C + \frac{1}{2} \text{Tr}(\mathbf{D}_1) \text{Tr}(\mathbf{D}_2) \right),$$

which induces the distance metric

$$\|\mathbf{D}_1 - \mathbf{D}_2\|_L = \sqrt{\frac{8\pi}{15} \left(\|\mathbf{D}_1 - \mathbf{D}_2\|_C^2 + \frac{1}{2} \text{Tr}^2(\mathbf{D}_1 - \mathbf{D}_2) \right)}.$$

Here we propose a new similarity measure that is based on comparing ADC profiles but it focuses on comparing only their anisotropic components. This is done by ignoring the $l=0$ term in the original L^2 inner product (6). Under the Gaussian model of diffusion, the new inner product, in terms of the diffusion tensors, becomes

$$\langle \mathbf{D}_1, \mathbf{D}_2 \rangle_D = \frac{8\pi}{15} \left(\langle \mathbf{D}_1, \mathbf{D}_2 \rangle_C - \frac{1}{3} \text{Tr}(\mathbf{D}_1) \text{Tr}(\mathbf{D}_2) \right),$$

which induces the distance metric

$$\|\mathbf{D}_1 - \mathbf{D}_2\|_D = \sqrt{\frac{8\pi}{15} \left(\|\mathbf{D}_1 - \mathbf{D}_2\|_C^2 - \frac{1}{3} \text{Tr}^2(\mathbf{D}_1 - \mathbf{D}_2) \right)}.$$

Interestingly, this metric is precisely the Euclidean distance between the respective deviatoric tensors of \mathbf{D}_1 and \mathbf{D}_2 (modulo the constant multiplier $\sqrt{8\pi/15}$) (Alexander and Gee, 2000). The deviatoric tensor of a tensor \mathbf{D} is the anisotropy part of \mathbf{D} and is defined as $\mathbf{D} - \frac{1}{3}\text{Tr}(\mathbf{D})\mathbf{I}$ with \mathbf{I} being the identity tensor. This means that the anisotropy parts of a ADC profile and its corresponding diffusion tensor contain essentially identical information.

3.2. Formulating tensor reorientation

Under rigid transformations of diffusion tensor images, tensor reorientation is well-defined. As illustrated in Fig. 2(c), this involves applying the rotational component of the rigid transformation to each tensor. Let the orthogonal matrix Q denote the rotational component of a rigid transformation. (For Q to represent physical rotations, Q should be special orthogonal, i.e., its determinant should be +1.) The action of the reorientation operator R on a diffusion tensor \mathbf{D} is then

$$R[\mathbf{D}] = Q\mathbf{D}Q^T. \quad (7)$$

To formulate the reorientation effect of general transformations, it suffices to understand the reorientation effect of affine transformations, because by using the Jacobian of a transformation at each voxel we can establish a local affine model of the voxel's neighborhood. By making the fundamental assumption that image transformations affect only the orientation (eigenvectors), but not the shape (eigenvalues) of the diffusion tensor, Alexander et al. (2001) further reduce the problem of tensor reorientation into the problem of finding for each tensor an orthogonal matrix with which the reorientation can be applied using Eq. (7). They observe that diffusion characterized by diffusion tensor is a property of the tissue microstructure. Although the change in the tissue orientation affects the tensor orientation, the change in shape or extent of the tissue region should not alter its microstructure, thus not the shape of the diffusion tensor.

Alexander et al. (2001) proposed several simple “reorientation strategies” to determine the orthogonal matrix Q from the Jacobian matrix M of some affine (or locally affine) transformation. The most widely used reorientation strategy from Alexander et al. (2001) is the “preservation of principal directions” (PPD) algorithm which addresses the particular importance of the reorientation of \mathbf{e}_1 , the original orientation of the diffusion tensor. Because \mathbf{e}_1 provides an estimate of the local fiber orientation and its image under M provides the estimate to the orientation of the transformed fiber, the first constraint that the PPD algorithm imposes on Q is that $Q\mathbf{e}_1 = \mathbf{n}_1$ where $\mathbf{n}_i = M\mathbf{e}_i / \|M\mathbf{e}_i\|$ is the normalized image of \mathbf{e}_i under M . The second constraint on Q is that $Q\mathbf{e}_2$ is as close to \mathbf{n}_2 as possible and can be satisfied by setting $Q\mathbf{e}_2 = \mathbf{m} / \|\mathbf{m}\|$ where $\mathbf{m} = \mathbf{n}_2 - (\mathbf{n}_1 \cdot \mathbf{n}_2)\mathbf{n}_1$. Fig. 4(b) illustrates the PPD reorientation applied to the image in Fig. 4(a) under a shearing transformation. A less accurate algorithm in Alexander et al. (2001) is the “finite strain” (FS) strategy. The FS algorithm selects the best orthogonal approximation of M to be Q , that is, Q is the solution of $\text{argmin}_Q \|Q' - M\|$ which is equal to $M / \sqrt{MM^T}$. Fig. 4(c) shows the same slice as in Fig. 4(b) but each tensor is reoriented using the FS algorithm instead. Alexander et al. (2001) showed that ignoring the dependency on the original orientation of the diffusion tensor makes the FS strategy less accurate compared to PPD (Alexander et al., 2001). However, when the deformation component of M , $\sqrt{MM^T}$, is small, the FS reorientation is a good approximation to PPD. Furthermore, in the framework of our algorithm, the FS strategy is simpler to compute than PPD and is analytic rather than algorithmic so that derivatives can be computed analytically.

3.3. Affine registration algorithm

The unique feature of our affine registration algorithm (Zhang et al., 2004) is that the tensor reorientation is incorporated into the analytic objective function for explicit orientation optimization, i.e., the search for the optimal reorientation of each tensor becomes part of the overall optimization. This is accomplished by parameterizing the

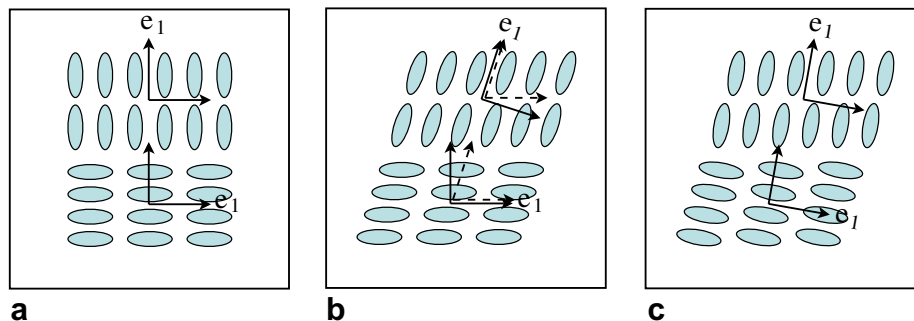


Fig. 4. The PPD and FS reorientation. Panel (a) shows schematically an axial slice in an anisotropic region of a DT-MR image. Panel (b) shows the same slice after a shear along the x -axis with each tensor reoriented using the PPD algorithm. The images of the original eigenvectors under the shear are shown in dotted arrows. Panel (c) shows the slice after the same shear, but with each tensor reoriented using the FS algorithm.

Jacobian matrix M of an affine transformation in terms of the polar decomposition of M and using the FS strategy for tensor reorientation.

The polar decomposition divides a non-singular matrix M into an orthogonal matrix Q (the pure rotation) and a symmetric positive definite matrix S (the pure deformation), such that $M = QS$. (Since M represents the Jacobian matrix of some physical transformation and therefore has a positive determinant, Q is guaranteed to be a rotation matrix.) Our algorithm relies on two important properties of this decomposition. Firstly, the relation between M and its decomposition is a bijection (Gallier, 2000). Thus we can parameterize M uniquely in terms of its polar decomposition. Secondly, the pure rotation Q is precisely the best orthogonal approximation to M . Hence, Q is precisely the solution to the FS reorientation strategy.

In the framework of our method, FS reorientation has two advantages over PPD reorientation. First, the rotation in FS reorientation is analytic in terms of M whereas the PPD rotation is algorithmic and has no closed-form expression. Second, FS reorientation is automatically determined via affine parameterization, while PPD reorientation requires eigen-decomposition, thus computationally more expensive.

By expressing an affine transformation F as $(QS)\mathbf{x} + \mathbf{T}$, the similarity term for some region Ω is then

$$\phi(\mathbf{p}) = \int_{\Omega} \|\mathbf{I}_s((QS)\mathbf{x} + \mathbf{T}) - Q\mathbf{I}_t(\mathbf{x})Q^T\|^2 d\mathbf{x}, \quad (8)$$

where $\mathbf{p} = (\mathbf{q}, \mathbf{s}, \mathbf{t})$, \mathbf{q} is the 3 Euler angles parameterizing Q , \mathbf{s} is the 6 independent components of S and $\mathbf{t} = \mathbf{T}$. The derivatives of $\phi(\mathbf{p})$ can be computed analytically as shown in Appendix A.

3.4. Piecewise affine algorithm

The piecewise algorithm we propose involves using our affine algorithm for region-wise matching, enforcing the overall smoothness of the warp via smoothness constraints on interfaces of regions.

We subdivide the template \mathbf{I}_t into equal-size regions denoted by Ω_i . In general, each region, Ω_i , has 6 neighboring regions and thus 6 different interfaces. For each region Ω_i in the template, the goal of the piecewise algorithm is to find an affine transformation F_i that gives the best match with the subject, under certain smoothness constraints that are described below. A 2D illustration is shown in Fig. 5.

We will refer to the collection of F_i over all possible regions as a piecewise affine transformation, denoted as \mathbb{F} . Because the transformation within each region is affine, the smoothness within a region is guaranteed. The smoothness of the piecewise affine transformation thus needs to be imposed only on region interfaces. Following the standard approach in optical flow estimation (Hellier et al., 2001), we minimize the transformation discontinuities across interfaces, which is formulated for neighboring regions Ω_i and Ω_j as

$$\psi(\mathbf{p}_i, \mathbf{p}_j) = \int_{\Omega_i \cap \Omega_j} \|F_i(\mathbf{x}) - F_j(\mathbf{x})\| d\mathbf{x}, \quad (9)$$

where \mathbf{p}_i and \mathbf{p}_j parametrize F_i and F_j , respectively. Similar to (8), analytic derivatives can be derived for (9) as shown in Appendix B.

If the number of regions in each dimension is n , the parameter space of this optimization problem has a dimension of $12n^3$. We subdivide the template hierarchically with n being 4, 8, 16 and 32. At the finest subdivision level, the

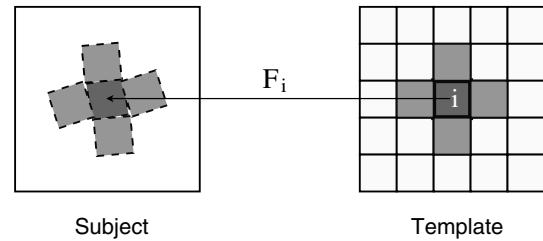


Fig. 5. A 2D illustration of the template being uniformly subdivided into contiguous regions. The neighbors to the region which is indexed by i and colored black are identified by light grey coloring.

$$F(\mathbf{x}) = \sum_{i=1}^4 w_i F_i(\mathbf{x})$$

$$w_1 = (1 - f(\lambda_1))(1 - f(\lambda_2))$$

$$w_2 = f(\lambda_1)(1 - f(\lambda_2))$$

$$w_3 = (1 - f(\lambda_1))f(\lambda_2)$$

$$w_4 = f(\lambda_1)f(\lambda_2)$$

$$f(\lambda) = \begin{cases} 0, & \text{if } 0 \leq \lambda < 0.25; \\ 1 - \cos((2\lambda - 0.5)\pi), & \text{if } 0.25 \leq \lambda \leq 0.75; \\ 1, & \text{if } 0.75 < \lambda \leq 1.0. \end{cases}$$

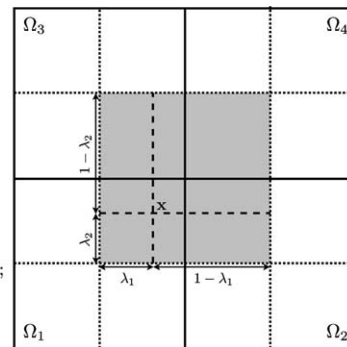


Fig. 6. A 2D illustration of the interpolation scheme used to produce a smooth deformation from a piecewise affine transformation. The vertices of the grey square are the centers of the four neighboring regions, Ω_{1-4} . The formulas describe the construction of the transformation at a given point within the grey square, F , as an interpolation of the affine transformations of the regions, F_{1-4} .

dimension of the parameter space is 393,216. The ability to compute derivatives of (9) analytically allows us to take advantage of the conjugate gradient method. Analytic derivative-based optimization is generally more efficient than optimization techniques that approximate derivatives with finite-difference method. The high dimensionality of our optimization problem makes optimization techniques

not using derivatives, such as the Powell's direction set (Press et al., 1993), impractical.

By construction, discontinuities across interfaces in the piecewise affine transformation can be minimized but not eliminated. Therefore, after the piecewise affine approximation to the underlying transformation is estimated at the finest level, it is interpolated using the standard approach

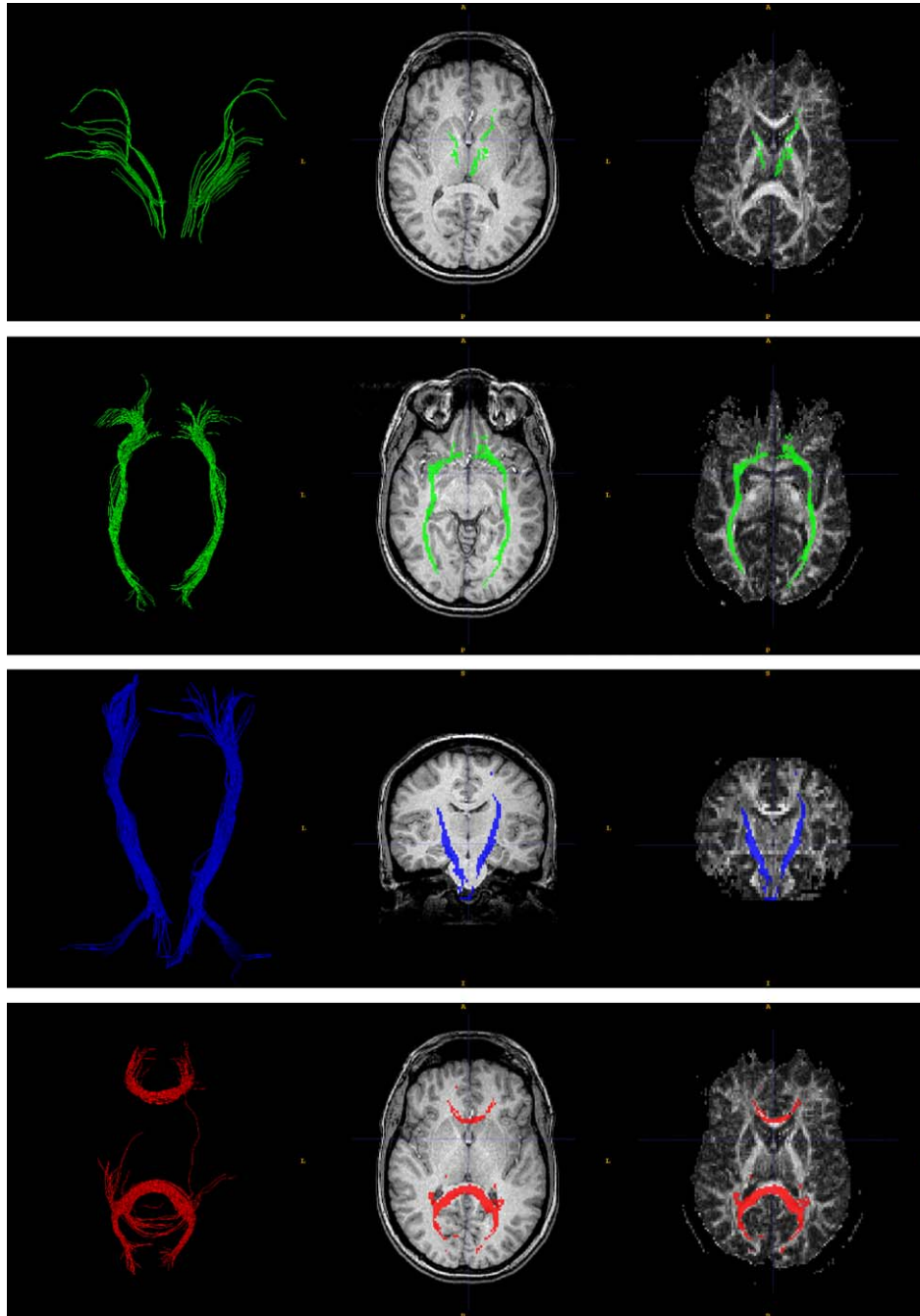


Fig. 7. The illustration of the white matter structures examined in this work. The illustrated fiber bundles were derived from the template. From top to bottom, they are the anterior thalamic radiations (ATR), the inferior fronto-occipital fasciculi (IFO), the corticospinal/corticobulbar tracts (CST), and the genu and the splenium of the corpus callosum (CC). The left column shows the 3D rendering of the fiber bundles. The center and right columns display the projection of the bundles onto structural and diffusion fractional anisotropy images, respectively. The long-association fibers are colored green, projection fibers blue and commissural fibers red. (For interpretation of the references to colour in this figure legend, the reader is referred to the Web version of this article.)

(Little et al., 1997) to generate a smooth warp field which is then used to deform the subject into the space of the template with the PPD reorientation. The interpolation scheme is illustrated in Fig. 6.

4. Evaluation

To evaluate our proposed deformable algorithm, we apply it to spatially normalize a set of DT-MR images to

an additional image chosen as the template. The algorithm is assessed by its effectiveness in aligning anatomically corresponding white matter structures of pairs of images and by the quality of the spatial normalizations with the normalized images analyzed as a whole. The results from our deformable algorithm are compared with affine registration results.

In the following, we first describe the subjects and data acquisition details pertaining to the MR images used in our

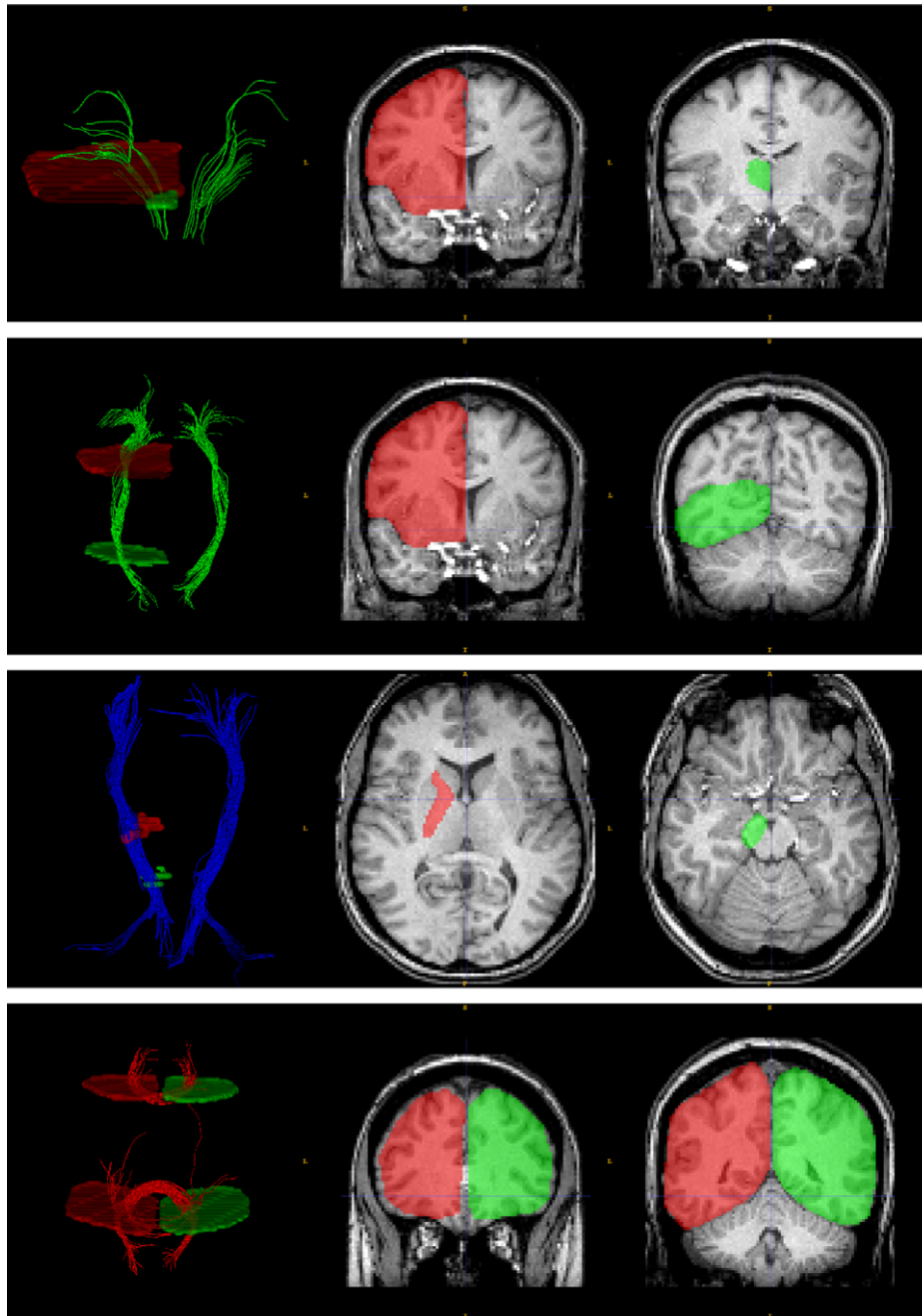


Fig. 8. The illustration of the ROIs defined for the template. Each row consists of a 3D rendering of a pair of ROIs overlaid with the fiber bundle which they were drawn to extract, and the 2D views of the ROIs overlaid with the structural image of the template. From top to bottom, the ROIs were defined for the ATRs, the IFOs, the CSTs and the genu/splenium of the CC. For the ATRs, the IFOs and the CSTs, the ROIs for only one hemisphere are shown. The two ROIs for both the genu and the splenium of the CC are defined in one coronal slice, thus each pair are shown together: the ones for the genu in the bottom center, the ones for the splenium to the bottom right.

evaluation. The details of registering the DT-MR images are then described. Our scheme for evaluating the alignment of two anatomically corresponding white matter structures is explained next. The criteria for assessing the spatial normalization are discussed in the end.

4.1. Subjects and data acquisition

Nine healthy subjects, with a mean age of 23 (range = 19–30), were recruited from the community served by the University of Pennsylvania Health System (UPHS), Philadelphia, PA. This research was approved by the local Institutional Review Board of the UPHS, and all subjects signed written informed consent prior to participation. Magnetic resonance imaging was performed on a 3.0-T Siemens Trio scanner (Siemens Medical Solutions, Erlangen, Germany). For each subject, a high-resolution three-dimensional structural MRI and a diffusion tensor MRI were obtained. The structural MRI was acquired using a T1-weighted magnetization prepared rapid gradient echo (MP-RAGE) sequence with the following scanning parameters: repetition time (TR) 1620 ms,

echo time (TE) 3.87 ms, 15° flip angle, number of averages = 1, matrix size = 256×192 , slice thickness of 1.0 mm, spacing between slices of 1.0 mm, yielding 160 axial slices with in-plane resolution of 0.98×0.98 mm. A single-shot, spin-echo, diffusion-weighted echo-planar imaging (EPI) sequence was used for the diffusion tensor MRI. The diffusion scheme was as follows: one image without diffusion gradients ($b = 0$ s/mm²), hereafter referred to as the $[b = 0]$ image, followed by 12 images measured with 12 non-collinear and non-coplanar diffusion encoding directions isotropically distributed in space ($b = 1000$ s/mm²). Additional imaging parameters for the diffusion-weighted sequence were: TR = 6500 ms, TE = 99 ms, 90° flip angle, number of averages = 6, matrix size = 128×128 , slice thickness = 3.0 mm, spacing between slices = 3.0 mm, 40 axial slices with in-plane resolution of 1.72×1.72 mm.

4.2. Spatial normalization of diffusion tensor images

The diffusion tensor images were reconstructed from their associated diffusion-weighted images that were first resampled to the voxel space of $128 \times 128 \times 64$ with the

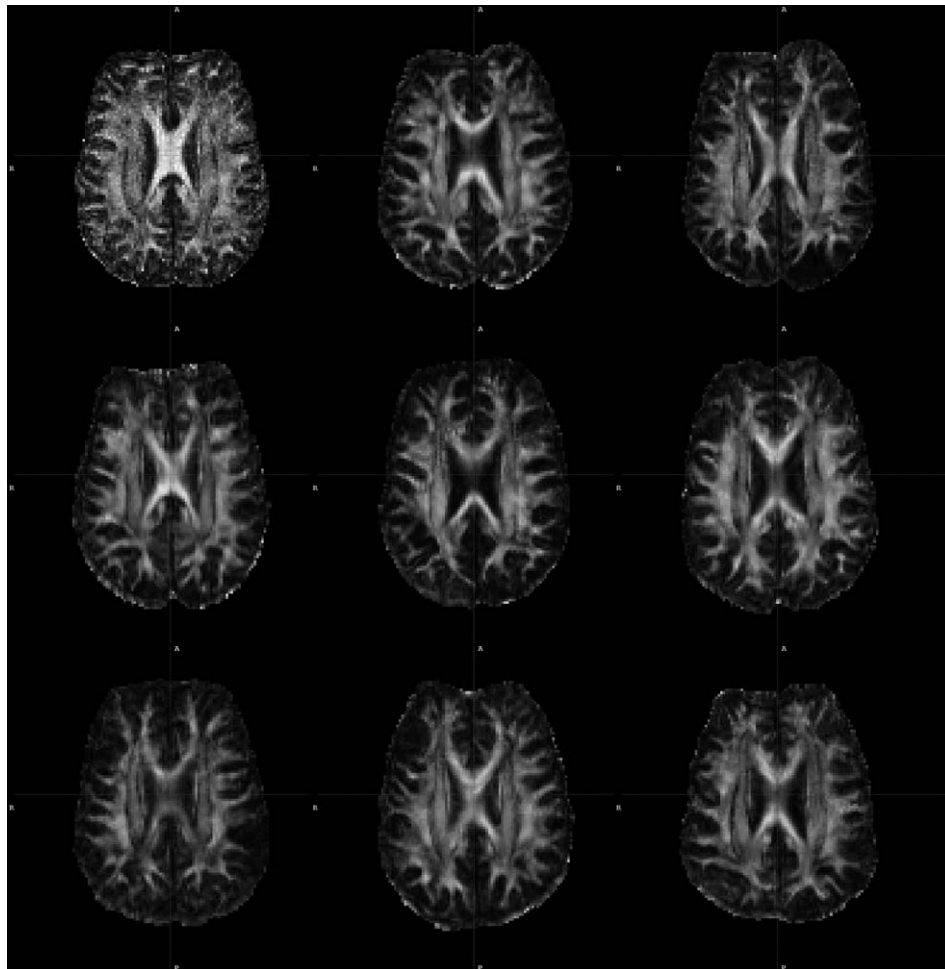


Fig. 9. For illustrative purposes, the 39th axial slice from the fractional anisotropy map (with a total of 64 axial slices) calculated from the diffusion tensor image of each subject is shown. The top-left image is from the subject chosen as the template. The rest of the images are from the other 8 subjects after normalized to the template with affine registration.

voxel spacing being $1.72 \times 1.72 \times 2.0$ mm. The new voxel space is more suitable for the hierarchical subdivision scheme of our deformable algorithm. One of the diffusion tensor images was arbitrarily designated as the template. The other 8 images made up the group to be spatially normalized. These images were first registered to the template with our affine registration algorithm for diffusion tensor images (Zhang et al., 2004). The affinely aligned images were then registered to the template with our deformable algorithm. The metric used in the deformable algorithm is the proposed metric based on comparing only anisotropic part of the ADC profiles described in Section 3.

4.3. Scheme for evaluating white matter alignment

Fiber bundles reconstructed with deterministic streamline-based tractography methods (Basser et al., 2000; Mori and van Zijl, 2002) are a desirable representation of white matter structures because they have been shown to demonstrate great consistency with the structure of the axonal fiber bundles observed in postmortem studies, particularly

for major white matter tracts (Wakana et al., 2004). Therefore, we propose to evaluate the alignment of two white matter structures by measuring the distance between their corresponding fiber bundles derived from tractography.

4.3.1. Generation of fiber bundles

To ensure that we compare white matter structures that are anatomically corresponding, we carefully selected a set of white matter tracts that are readily identifiable and whose fiber bundles can be derived reliably with tractography. The set of white matter tracts chosen were as follows: the anterior thalamic radiation (ATR) and the inferior fronto-occipital fasciculus (IFO) from the family of long-association fibers connecting different cortical areas; the corticospinal/corticobulbar tracts (CST) from the family of projection fibers connecting the cortex with the brainstem; the genu and the splenium of the corpus callosum from the family of commissural fibers bridging inter-hemispheric communication. Long-association fibers and projection fibers exist in both hemispheres of the brain. Therefore the ATRs, the IFOs and the CSTs from both

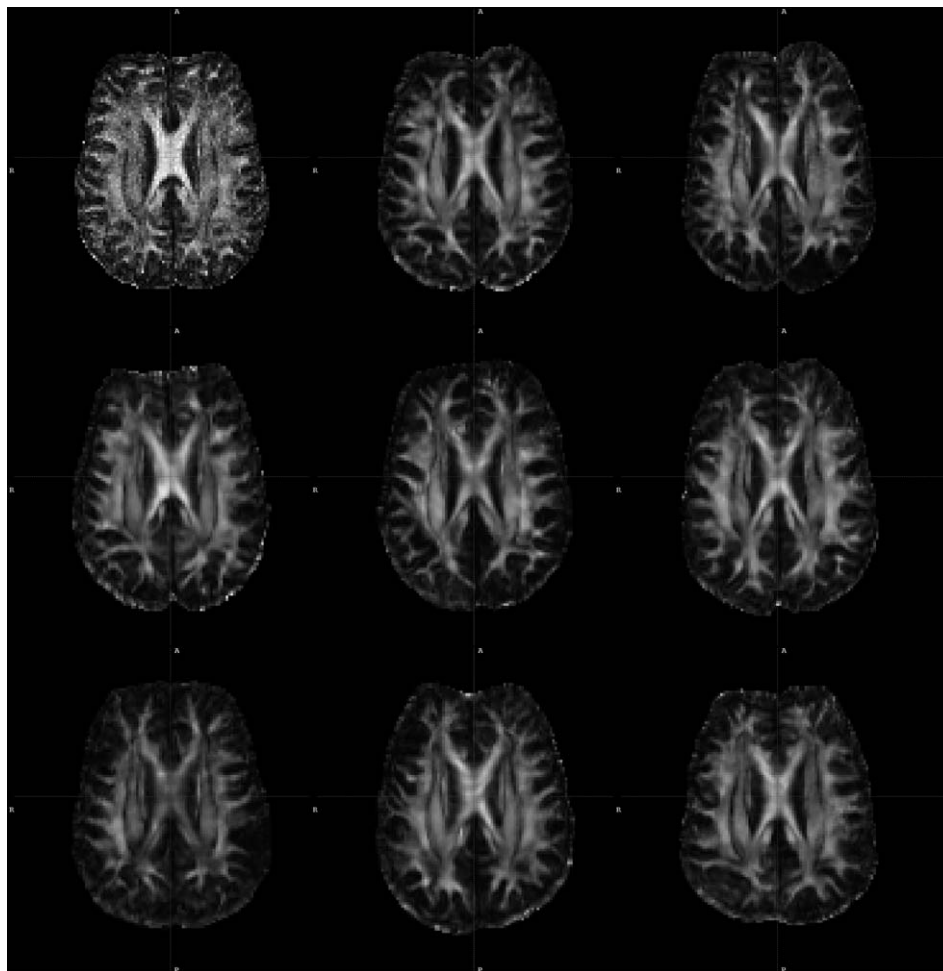


Fig. 10. For illustrative purposes, the 39th axial slice from the fractional anisotropy map (with a total of 64 axial slices) calculated from the diffusion tensor image of each subject is shown. The top-left image is from the subject chosen as the template. The rest of the images are from the other 8 subjects after normalized to the template with the deformable algorithm.

sides of the brain were included. These structures are illustrated in Fig. 7.

These fiber bundles were generated according to the protocols proposed in Stieltjes et al. (2001), Mori et al. (2002) and Wakana et al. (2004). Briefly, the fiber bundles are reconstructed from diffusion tensor images using a deterministic streamline tractography method known as FACT (Mori et al., 1999; Xue et al., 1999), with a fractional anisotropy threshold of 0.15 and an inner product threshold of 0.8, which prevents angles larger than 37° during tracking. A fiber was tracked from the center of any voxel with a fractional anisotropy above 0.2. The fiber bundles of interest were extracted from the fiber bundles of the whole brain using multiple-region-of-interest (ROI) approach (Stieltjes et al., 2001; Mori et al., 2002; Catani et al., 2002), which leverages existing anatomic knowledge of tract trajectories.

For the fiber bundles examined in this work, each was extracted using two ROIs (Stieltjes et al., 2001; Mori et al., 2002; Wakana et al., 2004). Using the segmentation tool ITK-SNAP (<http://www.itksnap.org>) (Yushkevich

et al., 2006), these ROIs were manually delineated for each of the 9 subjects, with the guidance of anatomical landmarks that can be identified with relative ease and consistency in structural images. The ROIs were drawn as polygons either in the coronal plane (for extracting both long-association fibers and commissural fibers) or in the axial plane (for projection fibers). To ensure that the relative orientation of the ROIs with respect to their subjects were consistent across multiple subjects, we first oriented the structural images consistently by transforming them to the same stereotactic space. This is accomplished using the spatial normalization tool in SPM2 (Wellcome Department of Cognitive Neurology, London, UK, <http://www.fil.ion.ucl.ac.uk/spm>) (Friston and Holmes, 1995). The transformations mapping the individual structural images to the standard space defined by the SPM2 template were affine and they were estimated by minimizing the residual sum of squared differences (Friston et al., 1995; Ashburner et al., 1997). Finally, the ROIs of each subject were transformed to the space of its diffusion tensor image by the inverse of the affine transformation that mapped its

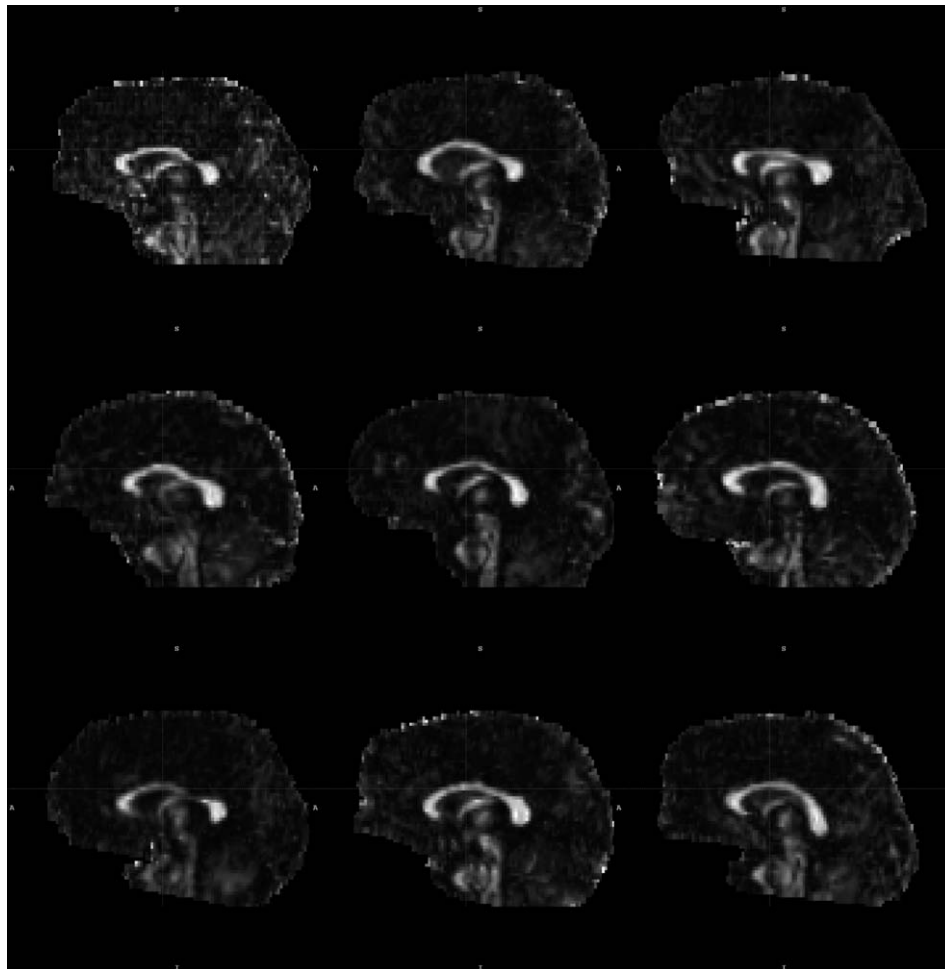


Fig. 11. For illustrative purposes, the 62th sagittal slice from the fractional anisotropy map (with a total of 128 sagittal slices) calculated from the diffusion tensor image of each subject is shown. The top-left image is from the subject chosen as the template. The rest of the images are from the other 8 subjects after normalized to the template with affine registration.

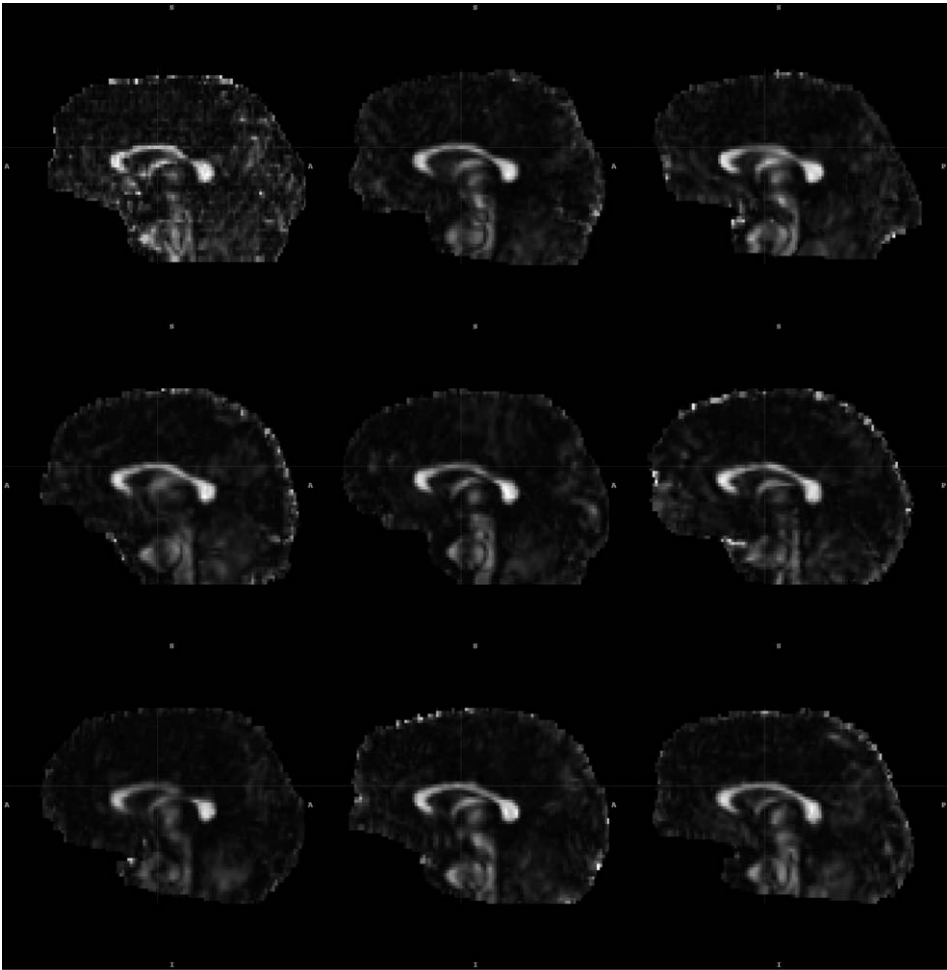


Fig. 12. For illustrative purposes, the 62th sagittal slice from the fractional anisotropy map (with a total of 128 sagittal slices) calculated from the diffusion tensor image of each subject is shown. The top-left image is from the subject chosen as the template. The rest of the images are from the other 8 subjects after normalized to the template with the deformable algorithm.

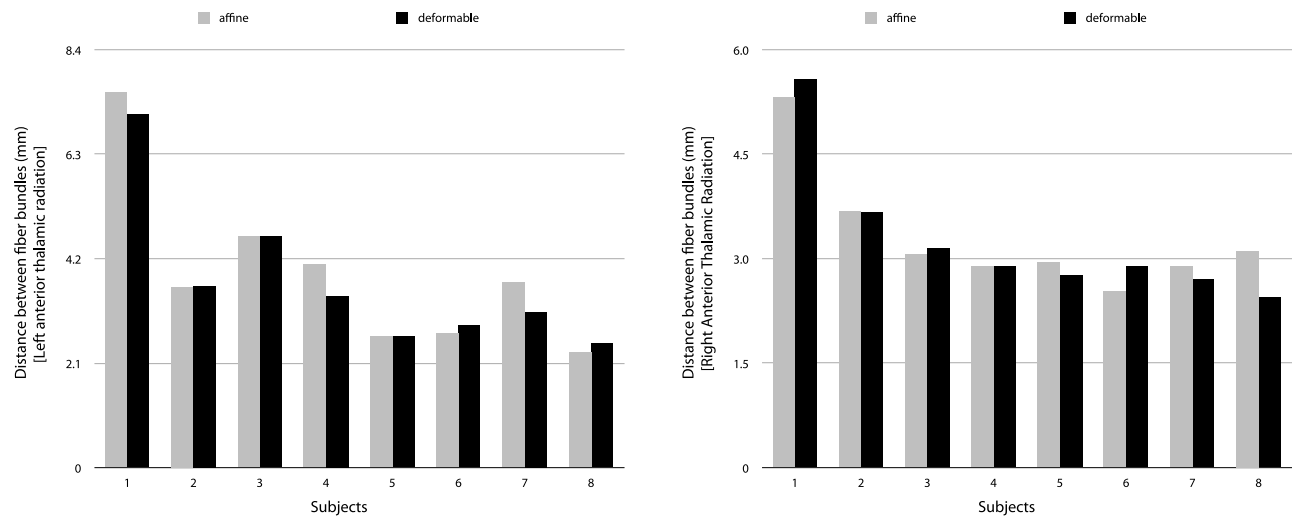


Fig. 13. The comparison of the alignment of the individual ATRs from the 8 subjects to the ATRs from the template both after affine registration and after deformable registration.

structural image to the stereotactic space and by the transformation coregistering its structural image to its $[b=0]$ image. The latter transformation was estimated with the coregistration tool within SPM2, which finds a rigid transformation that minimizes a normalized mutual information metric (Studholme et al., 1998). Fig. 8 demonstrates these ROIs delineated for the template, along with the fiber bundles extracted.

For the tractography, the diffusion tensor images were reconstructed from the original un-resampled diffusion-weighted images and were not manipulated in any other way, thereby avoiding the introduction of any tensor interpolation or tensor reorientation artifacts. To produce the fiber bundles corresponding to a spatially warped diffusion tensor image, we instead warped the tractography-derived

fiber bundles of the original diffusion tensor image with the transformation mapping the original diffusion tensor image to the warped space as in Xu et al. (2002, 2003).

4.3.2. Computing distances between fiber bundles

Using the notations in Gerig et al. (2004), we denote a fiber bundle as $\mathcal{F} = \{F_i, F_i = \{\mathbf{p}_k\}\}$ where F_i is the i th fiber, a 3D curve with a set of points \mathbf{p}_k . Given a pairwise distance between fibers, we considered the following three possible distance metrics for fiber bundles: the minimum, the mean and the maximum of the closest distances for every fiber of the two bundles. We chose to implement the mean of the closest distances since it provides an estimate that uses all the available data. It is more discriminative than the minimum of the closest distances and is less

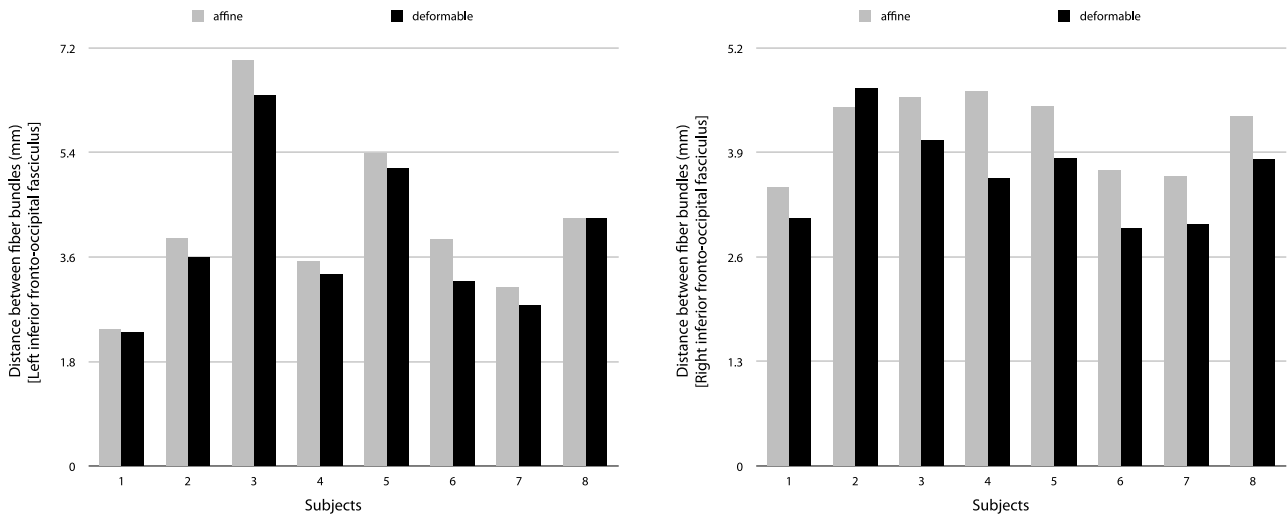


Fig. 14. The comparison of the alignment of the individual IFOs from the 8 subjects to the IFOs from the template both after affine registration and after deformable registration.

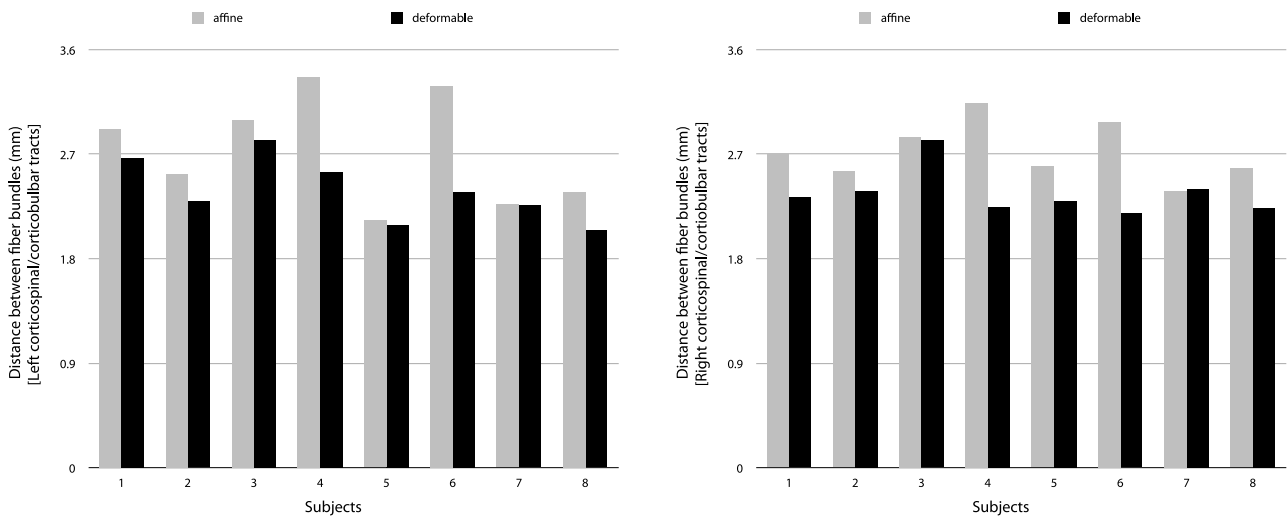


Fig. 15. The comparison of the alignment of the individual CSTs from the 8 subjects to the CSTs from the template both after affine registration and after deformable registration.

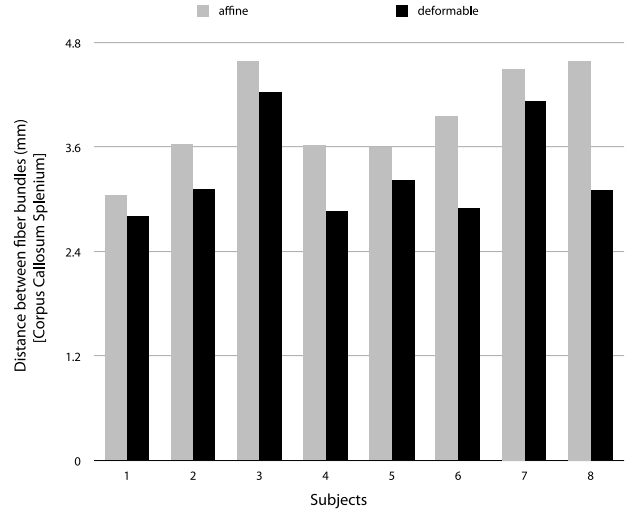
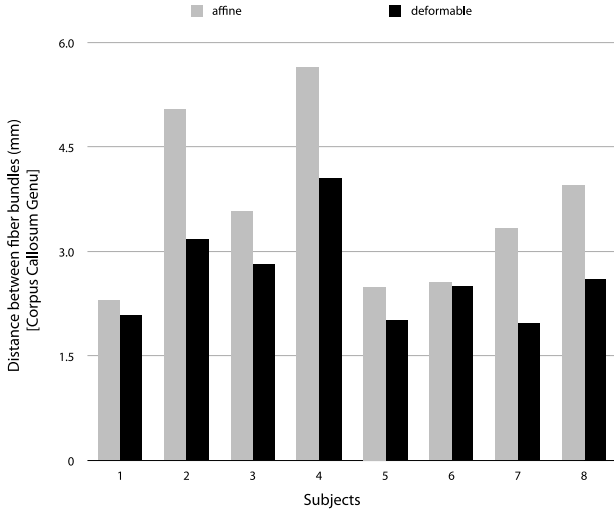


Fig. 16. The comparison of the alignment of the individual genu/splenium of the corpus callosum from the 8 subjects to the genu/splenium from the template both after affine registration and after deformable registration.

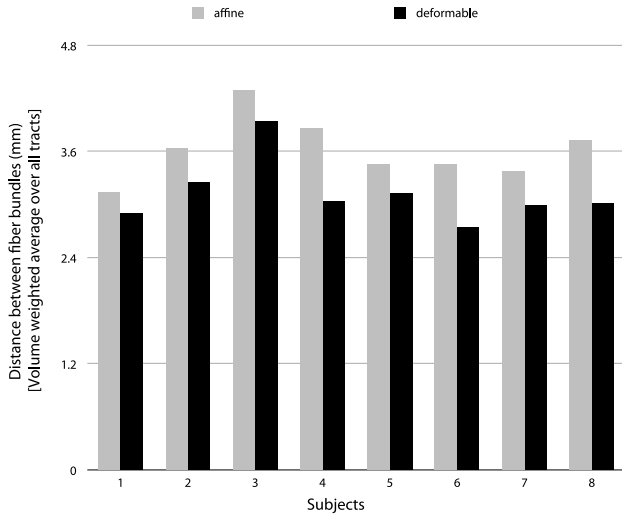


Fig. 17. The comparison of the overall alignment of all the white matter structures examined from the 8 subjects to those from the template both after affine registration and after deformable registration.

susceptible to the influence of outliers than the maximum of the closest distances, which is also known as the Hausdorff distance. Mathematically, let d be a pairwise distance between two fibers, we estimate the distance between two fiber bundles \mathcal{F} and \mathcal{G} as,

$$\frac{1}{|\mathcal{F}| + |\mathcal{G}|} \left(\sum_{F_i \in \mathcal{F}} \min_{G_j \in \mathcal{G}} d(F_i, G_j) + \sum_{G_j \in \mathcal{G}} \min_{F_i \in \mathcal{F}} d(F_i, G_j) \right), \quad (10)$$

where $\min_{G_j \in \mathcal{G}} d(F_i, G_j)$ is the distance between the fiber F_i and the fiber in \mathcal{G} that it is closest to and similarly $\min_{F_i \in \mathcal{F}} d(F_i, G_j)$ is the distance between the fiber G_j and the fiber in \mathcal{F} that it is closest to. Observe that the expression (10) is symmetric with respect to the two fibers involved and when two identical fiber bundles are perfectly aligned, it evaluates to zero.

The pairwise distance between fibers, d , that we chose to use in the expression (10) is similar to what is referred to by Gerig et al. (2004) as “the mean of closest distances”. It is defined as “the mean of the closest distance for every point of two fibers” (Gerig et al., 2004). Our implementation leverages the way we extracted the fiber bundles which allows us to approximately establish anatomic correspondence between points along fibers from different subjects as discussed in the following paragraph, as long as they were from the same white matter structure. Given the point-to-point correspondence between two fibers, we estimate the distance between them as the mean of the distance between corresponding points.

We establish the point-wise correspondence between fibers from two fiber bundles of the same white matter tract as follows. The two-ROI based fiber extraction allows us to identify a pair of points $\mathbf{p}_{a,b}$ on each fiber where it intersects with each of the ROIs. Given that the ROIs were defined to have anatomical correspondence across subjects and that the fiber bundles in question pass through the ROIs in tight clusters (relative to the length of the fiber bundles), we can assume that $\mathbf{p}_{a,b}$ from different subjects correspond to one another. Then we apply arc-length reparametrization to the fibers such that $\mathbf{p}_{a,b}$ remain on the reparametrized fibers and that the number of points between them are the same after reparametrization. This establishes an unambiguous point-wise correspondence between fibers. The two curve segments that flank the piece between $\mathbf{p}_{a,b}$ from different fibers in general do not have the matching number of points after the reparametrization and the unmatched points are not considered in the distance computation.

4.4. Criteria for assessing spatial normalization

Assessing spatial normalization of diffusion tensor images is less simple compared to similar analysis of

scalar-valued images. We will use two criteria proposed in Jones et al. (2002) that are designed for analyzing diffusion tensor images: normalized standard deviation of tensors and dyadic coherence. The first criterion quantifies, on a

voxel-by-voxel basis, the variability of tensors from the same voxel of a set of diffusion tensor images. Jones et al. (2002) defines the normalized standard deviation of tensors as

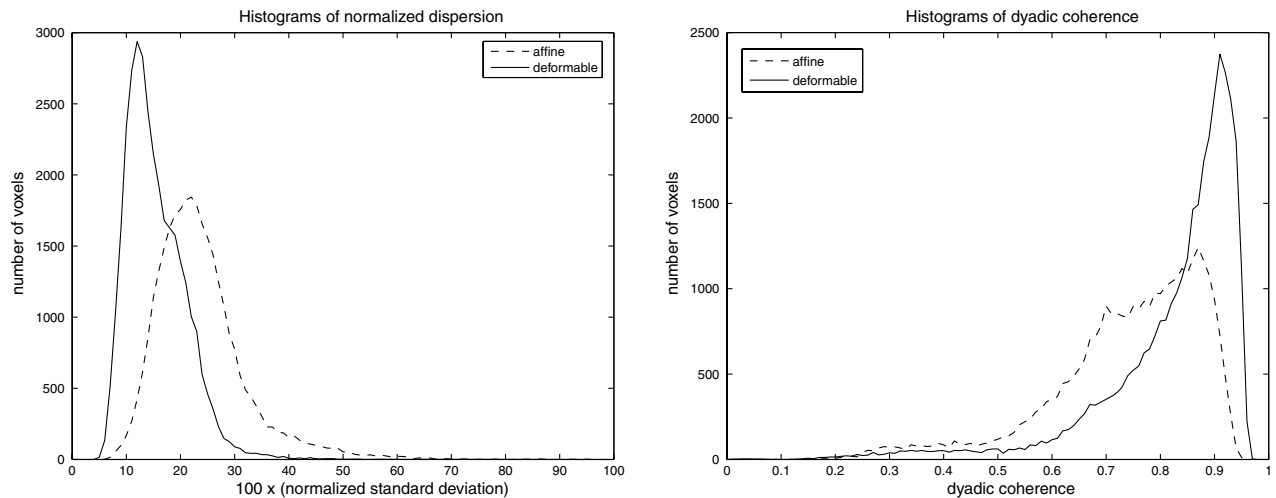


Fig. 18. The comparison of the affine normalized diffusion tensor images from the 8 subjects to those normalized with the deformable algorithm using the histograms of the normalized standard deviation of tensors and the dyadic coherence.

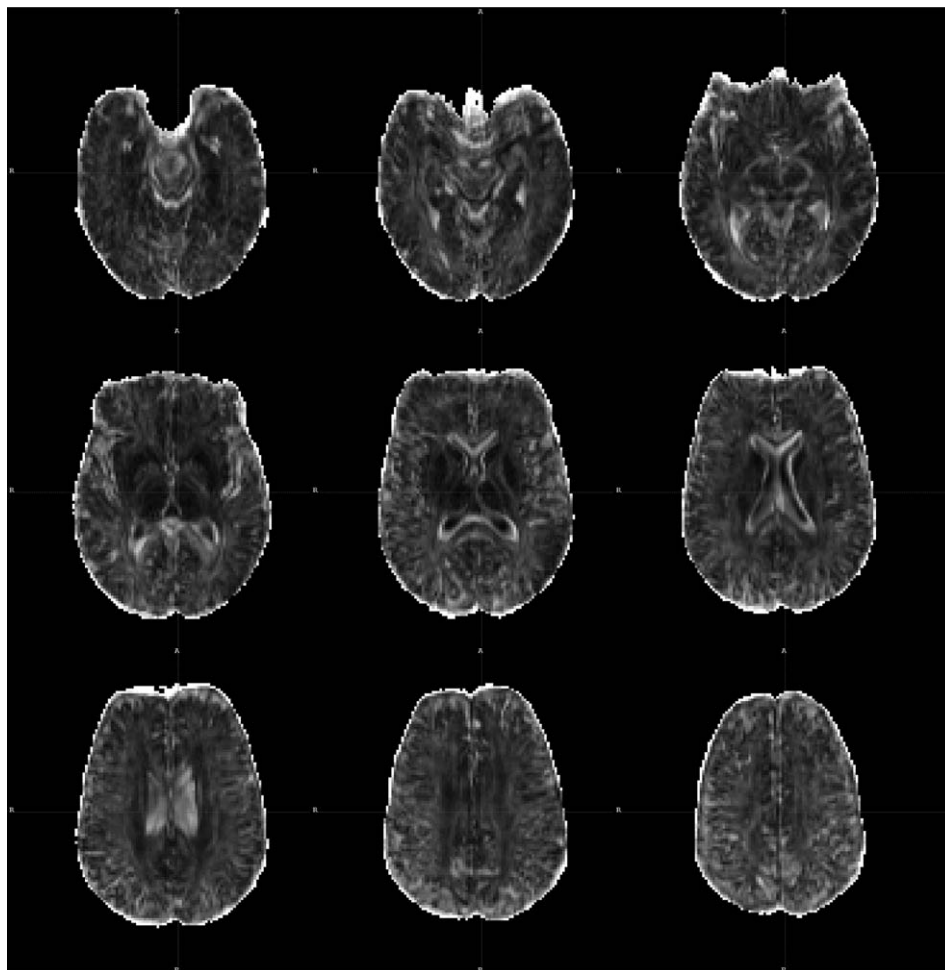


Fig. 19. Normalized standard deviation map derived from the set of diffusion tensor images normalized using affine registration, showing every fourth slice starting from slice 16 to slice 48 of the 64-slice image.

$$\frac{1}{\|\bar{\mathbf{D}}\|_C} \sqrt{\frac{1}{N-1} \sum_{k=1}^N \|\mathbf{D}_k - \bar{\mathbf{D}}\|_C^2}, \quad (11)$$

where $\bar{\mathbf{D}}$ is the mean of the set of tensors from the same voxel of a set of N diffusion tensor images and \mathbf{D}_k is the tensor from the k th image. The mean tensor $\bar{\mathbf{D}}$ is computed by component-wise averaging of the tensors, $\{\mathbf{D}_k\}_{k=1,2,\dots,N}$. The second criterion estimates the variability of principal eigenvectors of tensors in each voxel of a set of diffusion tensor images. It is based on calculating the mean of dyadic tensors formed from principal eigenvectors of tensors (Basser and Pajevic, 2000). The dyadic tensor of a tensor is equal to $\mathbf{e}_1 \mathbf{e}_1^T$, the outer product of the principal eigenvector of the tensor. The mean dyadic tensor of a set of tensors is then computed as component-wise averaging of the respective dyadic tensors. Using the eigenvalues of the mean dyadic tensor, denoted as $\{\beta_i\}_{i=1,2,3}$ sorted in descending order, the dyadic coherence κ is defined as

$$1 - \sqrt{\frac{\beta_2 + \beta_3}{2\beta_1}}. \quad (12)$$

The dyadic coherence ranges from 0, when the different subjects' principal eigenvectors are oriented randomly, to 1, when the individual principal eigenvectors are identically aligned.

5. Results

For illustrative purposes, one axial slice and one sagittal slice of the FA maps from each of the 8 subjects both after affine registration and after deformable registration are shown in Figs. 9–12, respectively. The axial slice chosen shows the top of the corpus callosum midbody in the case of the template. Fig. 9 shows that affine registration failed to align this structure from the other subjects to the one of the template. Fig. 10 shows that affine registration failed to align this structure from the other subjects to the one of the template. The alignment of the midbody of the corpus callosum was greatly improved after the deformable registration as shown in Fig. 10. The sagittal slice is at the level of the inter-hemispheric fissure. Fig. 11 shows that affine registration could not remove the large variability in the shape of the corpus callosum. The overall length, curvature of the corpus callosum, the shape of the genu and the splenium vary significantly across subjects. The deformable

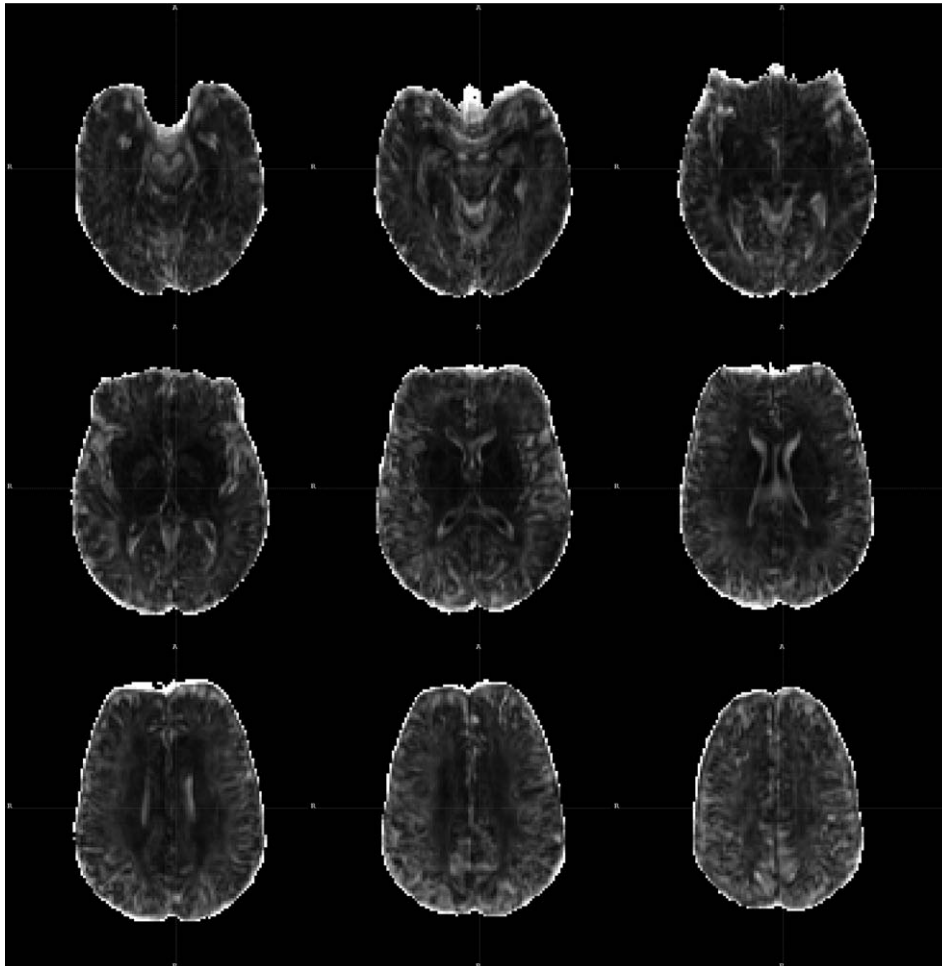


Fig. 20. Normalized standard deviation map derived from the set of diffusion tensor images normalized using deformable registration, showing every fourth slice starting from slice 16 to slice 48 of the 64-slice image. For illustrative purposes.

registration however was able to greatly reduce these shape variations as shown in Fig. 12.

The improved alignment with the deformable algorithm was confirmed quantitatively based on the analysis of the fiber bundle alignment as outlined in Section 4. Figs. 13–16 compare the white matter alignment after affine registration with after deformable registration. Except for the ATRs, the alignment of the different structures examined were improved for almost all subjects after deformable registration. We also computed the volume-weighted mean bundle distance, which is the weighted sum of the distances of all four structures with the weighting being proportional to the volume of each structure. The volume of each structure is approximated by the total number of voxels resulting from voxelizing the corresponding fiber bundle. The deformable algorithm reduced the volume-weighted mean bundle distances for all subjects as shown in Fig. 17.

The improved white matter structure alignment at the individual subject level was also reflected in the improved quality of spatial normalization. Fig. 18 shows the histograms of the normalized standard deviation of tensors and the dyadic coherence from the subjects after affine reg-

istration and after deformable registration respectively. To limit the comparison to white matter regions alone, the histograms were computed for the voxels with a fractional anisotropy of the mean tensor larger than 0.3. For affine registration, the normalized standard deviation histogram peaks close to 22% similar to the value reported in Jones et al. (2002). The normalized standard deviation histogram for the deformable algorithm shifts significantly towards 0 compared to the one for the affine registration, indicating lower tensor variability. In the case of dyadic coherence, the histogram of the images after deformable alignment peaks much closer to 1 compared to the histogram of the images after affine alignment, revealing better alignment of principal eigenvectors. To demonstrate the spatial distribution of the improved normalization revealed in Fig. 18, the maps of the normalized standard deviation derived from the set of diffusion tensor images normalized using affine and deformable registration are shown in Figs. 19 and 20, respectively. The corresponding dyadic coherence maps are shown in Figs. 21 and 22. The normalized standard deviation map of deformable registration compared to that of affine registration appears darker, i.e., lower in

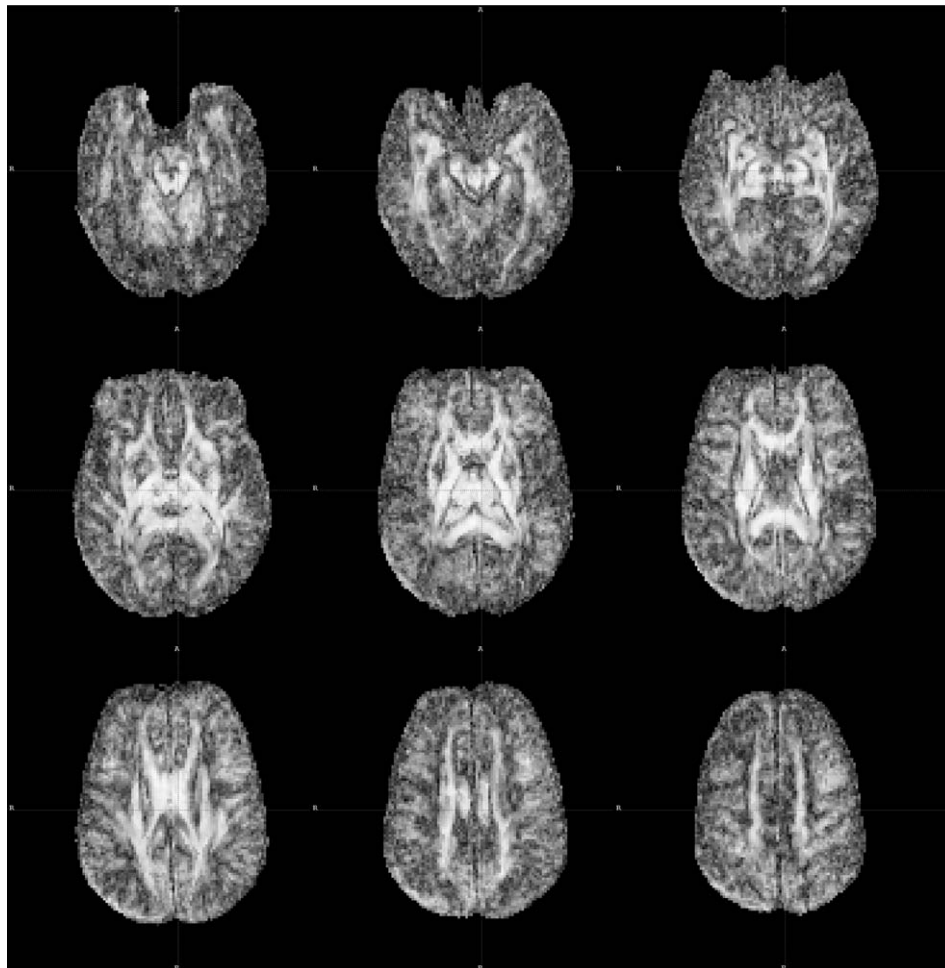


Fig. 21. Dyadic coherence map derived from the set of diffusion tensor images normalized using affine registration, showing every fourth slice starting from slice 16 to slice 48 of the 64-slice image.

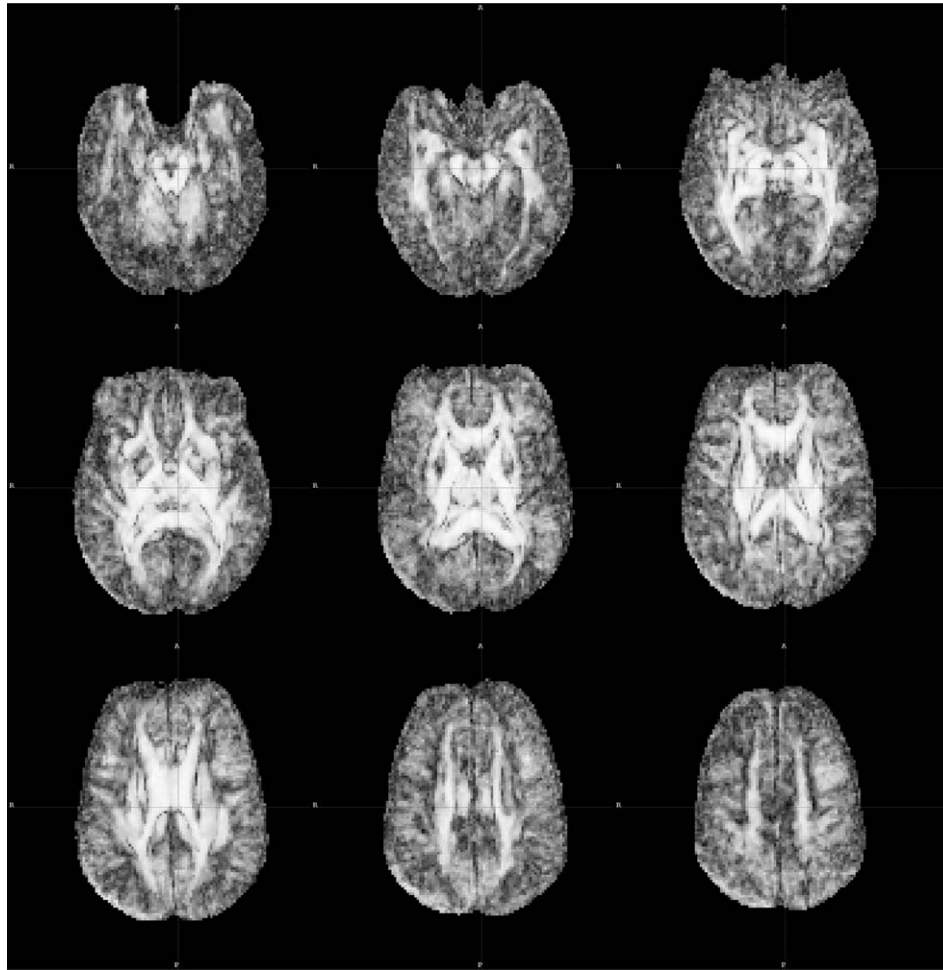


Fig. 22. Dyadic coherence map derived from the set of diffusion tensor images normalized using deformable registration, showing every fourth slice starting from slice 16 to slice 48 of the 64-slice image.

tensor variability, with the more pronounced reduction in internal white matter regions. The dyadic coherence map of deformable registration compared to that of affine registration features more and thicker bands of intense brightness, i.e., large coherence, in major white matter tracts. These observations further indicate that our deformable algorithm improves white matter alignment.

6. Discussion

Diffusion tensor images afford us unique insight into microscopic organization of white matter structures. Its sensitivity to microscopic differences in white matter, such as differences in axon myelination or axon fiber density, has made the modality a popular choice for imaging based study of white matter (Kubicki et al., 2002). Spatial normalization of diffusion tensor images is a prerequisite for studies that aim to explore unanticipated white matter differences between multiple groups of population. Despite the general consensus that registration algorithms based on matching tensors as a whole should improve the align-

ment of diffusion tensor images, the computational challenges presented by tensor reorientation have limited the development of such algorithms. Instead, spatial normalization of diffusion tensor images has generally been done by coregistering $[b = 0]$ images to the corresponding structural images and then relying on the normalization of the structural images (Xu et al., 2002, 2003). In this paper, we have addressed the unique challenge of registration using tensor-based metrics by presenting a method that incorporates tensor reorientation in an efficient manner. On a modern workstation, registering a diffusion tensor volume of size $128 \times 128 \times 64$, the run time of our proposed deformable algorithm is around 5 min, comparable to that of our affine algorithm (Zhang et al., 2004). We have demonstrated that our deformable algorithm improves white matter alignment upon affine registration both qualitatively and quantitatively. We have also shown that the improved registration at the individual subject level translates to the improved spatial normalization at the group level. Although it is beyond the scope of the current work, the comparison of the quality of spatial normalization of

the proposed method with the traditional one (Xu et al., 2002, 2003) could help us quantify the benefits from using tensor-based registration algorithms.

An additional contribution of this work is the quantification of the alignment of white matter structures in terms of their corresponding tractography-derived fiber bundles. Park et al. (2003) also proposed to use tractography-derived fiber bundles for the evaluation of white matter alignment. In Park et al. (2003) the fiber bundles from different subjects were tracked from the same set of seed points. To assess the alignment of two subjects, they computed the distances between the corresponding fibers tracked with the same seed points. Their motivation was that the fibers from different white matter structures are generally different in length and shape, thus if the fibers from different subjects passing through a common seed point are similar, it is likely the fibers belong to the same white matter structure. Compared to the method of Park et al. (2003), our scheme is different in that we compare the fiber bundles from anatomically corresponding white matter structures and allow us to assess the alignment of specific structures of interest. In addition, we did not need to generate fiber bundles in the warped diffusion tensor images using tractography as in Park et al. (2003), thus avoiding the introduction of fiber tracking errors due to artifacts in the warped images caused by tensor interpolation and reorientation. Our method, however, can not provide the same alignment assessment at the whole brain level as in Park et al. (2003).

As discussed in Section 3, there are a number of tensor-based metrics available. Our choice of deviatoric tensor-based metric is motivated by our earlier results (Zhang et al., 2005) which appeared to suggest that the more contribution isotropic components of diffusion tensors have in a metric, the less sensitive the metric is to match white matter structures. Further analysis would be required to conclude whether this is true in general or only applicable to our particular method.

The use of the FS tensor reorientation in our algorithm limits its application to small or finite deformation. Extending the current method to deal with large deformation is an ongoing research. A promising solution for large deformation tensor field matching was proposed by Cao et al. (2006) as an extension to their earlier work (Cao et al., 2005). Their algorithm uses PPD for tensor reorientation and in their framework, PPD can be written in closed-form and differentiated analytically.

Recent advances in tensor interpolation (Fletcher and Joshi, 2004; Pennec et al., 2004; Arsigny et al., 2005) suggest additional avenues for future research. Despite component-wise tensor interpolation has known issues (Fletcher and Joshi, 2004; Pennec et al., 2004; Arsigny et al., 2005), it is much faster and simpler to compute than the early alternatives (Fletcher and Joshi, 2004; Pennec et al., 2004). Most recently, however, Arsigny et al. (2005) introduced the Log-Euclidean framework for tensor interpolation; the new framework is particularly attractive

for interpolating tensors during image registration because of its fast and simple implementation. Comparing the effect of using different tensor interpolation schemes on registration is an important area of future research.

7. Conclusion

In conclusion, we have presented a piecewise affine algorithm that demonstrates explicit orientation optimization required for optimal matching of diffusion tensor images can be accommodated in deformable registration. Moreover, our novel formulation enables fast and accurate optimization using analytic derivatives. The proposed algorithm was evaluated by a novel scheme that assesses the alignment of anatomically corresponding white matter structures. Results from inter-subject registration demonstrate the algorithm improves image alignment upon affine registration.

Acknowledgements

The authors gratefully acknowledge support of this work by the USPHS through NIH grants NS044189, DA015886, HD042974, HD046159, and NS045839. We thank the members of PICS, particularly, Tessa Sundaram and Nick Tustison for offering comments and suggesting corrections to the early draft of this work.

Appendix A. Analytic derivatives of the affine objective function

Here we show the formulas for the derivatives of $\phi(p)$ (8). Recall that $\mathbf{p} = (\mathbf{q}, \mathbf{s}, \mathbf{t})$, where $\mathbf{q} = (\theta, \phi, \psi)$ and parametrizes the rotation matrix

$$\mathbf{Q} = \begin{pmatrix} \cos \phi & 0 & \sin \phi \\ 0 & 1 & 0 \\ -\sin \phi & 0 & \cos \phi \end{pmatrix} \begin{pmatrix} 1 & 0 & 0 \\ 0 & \cos \theta & \sin \theta \\ 0 & -\sin \theta & \cos \theta \end{pmatrix} \begin{pmatrix} \cos \psi & \sin \psi & 0 \\ -\sin \psi & \cos \psi & 0 \\ 0 & 0 & 1 \end{pmatrix}, \quad (\text{A.1})$$

$\mathbf{s} = (S_{11}, S_{21}, S_{22}, S_{31}, S_{32}, S_{33})$ and parametrizes the symmetric matrix

$$\mathbf{S} = \begin{pmatrix} S_{11} & S_{21} & S_{31} \\ S_{21} & S_{22} & S_{32} \\ S_{31} & S_{32} & S_{33} \end{pmatrix}, \quad (\text{A.2})$$

$\mathbf{t} = (x, y, z)$ and parametrizes the translation $\mathbf{T} = \mathbf{t}$.

Let \mathbf{x}' denote $(\mathbf{Q}\mathbf{S})\mathbf{x} + \mathbf{T}$, then the derivative with respect to q_i , the i th component of \mathbf{q} is

$$\begin{aligned} \frac{\partial \phi}{\partial q_i} = & \int_{\Omega} 2 \left\langle \sum_{j=1}^3 \frac{\partial \mathbf{I}_s(\mathbf{y})}{\partial y_j} \bigg|_{\mathbf{y}=\mathbf{x}'} \left(\left(\frac{\partial \mathbf{Q}}{\partial q_i} \mathbf{S} \right) \mathbf{x} \right)_j \right. \\ & \left. - \frac{\partial \mathbf{Q}}{\partial q_i} \mathbf{I}_t(\mathbf{x}) \mathbf{Q}^T - \mathbf{Q} \mathbf{I}_t(\mathbf{x}) \frac{\partial \mathbf{Q}^T}{\partial q_i}, \mathbf{I}_s(\mathbf{x}') - \mathbf{Q} \mathbf{I}_t(\mathbf{x}) \mathbf{Q}^T \right\rangle d\mathbf{x}, \end{aligned}$$

where $\frac{\partial \mathbf{Q}}{\partial q_i}$ can be derived from (A.1).

The derivative with respect to s_i , the i th component of \mathbf{s} is

$$\frac{\partial \phi}{\partial s_i} = \int_{\Omega} 2 \left\langle \sum_{j=1}^3 \frac{\partial \mathbf{I}_s(\mathbf{y})}{\partial y_j} \bigg|_{\mathbf{y}=\mathbf{x}'} \left(\mathcal{Q} \left(\frac{\partial S}{\partial s_i} \right) \mathbf{x} \right)_j, \mathbf{I}_s(\mathbf{x}') - \mathcal{Q} \mathbf{I}_t(\mathbf{x}) \mathcal{Q}^T \right\rangle d\mathbf{x},$$

where $\frac{\partial S}{\partial s_i}$ can be derived from (A.2).

The derivative with respect to t_i , the i th component of \mathbf{t} is

$$\frac{\partial \phi}{\partial t_i} = \int_{\Omega} 2 \left\langle \sum_{j=1}^3 \frac{\partial \mathbf{I}_s(\mathbf{y})}{\partial y_j} \bigg|_{\mathbf{y}=\mathbf{x}'} \left(\frac{\partial \mathbf{T}}{\partial t_i} \right)_j, \mathbf{I}_s(\mathbf{x}') - \mathcal{Q} \mathbf{I}_t(\mathbf{x}) \mathcal{Q}^T \right\rangle d\mathbf{x},$$

where $\frac{\partial \mathbf{I}_s(\mathbf{y})}{\partial y_j}$ is the spatial derivative of the tensor image \mathbf{I}_s along the spatial direction y_j . Note that $\left(\frac{\partial \mathbf{T}}{\partial t_i} \right)_j = \delta_{ij}$, thus the derivative can be simplified to

$$\frac{\partial \phi}{\partial t_i} = \int_{\Omega} 2 \left\langle \frac{\partial \mathbf{I}_s(\mathbf{y})}{\partial y_i} \bigg|_{\mathbf{y}=\mathbf{x}'}, \mathbf{I}_s(\mathbf{x}') - \mathcal{Q} \mathbf{I}_t(\mathbf{x}) \mathcal{Q}^T \right\rangle d\mathbf{x}.$$

Appendix B. Analytic derivatives of the smoothness term

Here we show the formulas for the derivatives of $\psi(\mathbf{p}_i, \mathbf{p}_j)$ (9). To simplify the formulas, we will rename \mathbf{p}_i and \mathbf{p}_j as $\mathbf{p} = (\mathbf{q}, \mathbf{s}, \mathbf{t})$ and $\mathbf{p}' = (\mathbf{q}', \mathbf{s}', \mathbf{t}')$, respectively, and $\psi(\mathbf{p}_i, \mathbf{p}_j)$ becomes

$$\begin{aligned} \psi(\mathbf{p}, \mathbf{p}') &= \int_{\Omega_{\mathbf{p}} \cap \Omega_{\mathbf{p}'}} \|F_{\mathbf{p}}(\mathbf{x}) - F_{\mathbf{p}'}(\mathbf{x})\| d\mathbf{x} \\ &= \int_{\Omega_{\mathbf{p}} \cap \Omega_{\mathbf{p}'}} \|\mathcal{Q}(\mathbf{q})S(\mathbf{s})\mathbf{x} + \mathbf{T}(\mathbf{t}) - \mathcal{Q}(\mathbf{q}')S(\mathbf{s}')\mathbf{x} \\ &\quad - \mathbf{T}(\mathbf{t}')\| d\mathbf{x} \end{aligned}$$

The derivative with respect to q_i , the i th component of \mathbf{q} is

$$\begin{aligned} \frac{\partial \psi}{\partial q_i} &= \int_{\Omega_{\mathbf{p}} \cap \Omega_{\mathbf{p}'}} \frac{1}{\|F_{\mathbf{p}}(\mathbf{x}) - F_{\mathbf{p}'}(\mathbf{x})\|} \\ &\quad \times \left\langle \frac{\partial \mathcal{Q}(\mathbf{q})}{\partial q_i} S(\mathbf{s})\mathbf{x}, F_{\mathbf{p}}(\mathbf{x}) - F_{\mathbf{p}'}(\mathbf{x}) \right\rangle d\mathbf{x}. \end{aligned}$$

The derivative with respect to s_i , the i th component of \mathbf{s} is

$$\begin{aligned} \frac{\partial \psi}{\partial s_i} &= \int_{\Omega_{\mathbf{p}} \cap \Omega_{\mathbf{p}'}} \frac{1}{\|F_{\mathbf{p}}(\mathbf{x}) - F_{\mathbf{p}'}(\mathbf{x})\|} \\ &\quad \times \left\langle \mathcal{Q}(\mathbf{q}) \frac{\partial S(\mathbf{s})}{\partial s_i} \mathbf{x}, F_{\mathbf{p}}(\mathbf{x}) - F_{\mathbf{p}'}(\mathbf{x}) \right\rangle d\mathbf{x}. \end{aligned}$$

The derivative with respect to t_i , the i th component of \mathbf{t} is

$$\frac{\partial \psi}{\partial t_i} = \int_{\Omega_{\mathbf{p}} \cap \Omega_{\mathbf{p}'}} \frac{1}{\|F_{\mathbf{p}}(\mathbf{x}) - F_{\mathbf{p}'}(\mathbf{x})\|} \left\langle \frac{\partial \mathbf{T}(\mathbf{t})}{\partial t_i}, F_{\mathbf{p}}(\mathbf{x}) - F_{\mathbf{p}'}(\mathbf{x}) \right\rangle d\mathbf{x}.$$

Because $\psi(\mathbf{p}, \mathbf{p}') = \psi(\mathbf{p}', \mathbf{p})$, the derivatives with respect to the components of \mathbf{p}' can be derived by swapping \mathbf{p} and \mathbf{p}' in the formulas for the derivatives with respect to the components of \mathbf{p} .

References

- Alexander, D.C., 2005. An introduction to computational diffusion MRI: the diffusion tensor and beyond. In: Welckert, J., Hagen, H. (Eds.), *Visualization and Image Processing of Tensor Fields*. Springer, Berlin.
- Alexander, D.C., Barker, G.J., Arridge, S.R., 2002. Detection and modeling of non-gaussian apparent diffusion coefficient profiles in human brain data. *Magn. Reson. Med.* 48 (2), 331–340.
- Alexander, D.C., Gee, J.C., 2000. Elastic matching of diffusion tensor images. *Comput. Vis. Image Understand.* 77 (2), 233–250.
- Alexander, D.C., Pierpaoli, C., Basser, P.J., Gee, J.C., 2001. Spatial transformations of diffusion tensor magnetic resonance images. *IEEE Trans. Med. Imag.* 20 (11), 1131–1139.
- Arsigny, V., Fillard, P., Pennec, X., Ayache, N., 2005. Fast and simple calculus on tensors in the Log-Euclidean framework. In: *Proceedings of the MICCAI*.
- Ashburner, J., Neelin, P., Collins, D.L., Evans, A.C., Friston, K.J., 1997. Incorporating prior knowledge into image registration. *NeuroImage* 6, 344–352.
- Basser, P.J., Mattiello, J., Bihan, D.L., 1994. Estimation of the effective self-diffusion tensor from the NMR spin echo. *J. Magn. Reson.* 103, 247–254.
- Basser, P.J., Pajevic, S., 2000. Statistical artifacts in diffusion tensor MRI (DT-MRI) caused by background noise. *Magn. Reson. Med.* 44, 41–50.
- Basser, P.J., Pajevic, S., Pierpaoli, C., Duda, J., Aldroubi, A., 2000. In vitro fiber tractography using DT-MRI data. *Magn. Reson. Med.* 44, 625–632.
- Cao, Y., Miller, M., Mori, S., Winslow, R.L., Younes, L., 2006. Diffeomorphic matching of diffusion tensor images. In: *Proceedings of the MMBIA*.
- Cao, Y., Miller, M., Winslow, R.L., Younes, L., 2005. Large deformation diffeomorphic metric mapping of vector fields. *IEEE Trans. Med. Imag.* 24 (9), 1216–1230.
- Catani, M., Howard, R.J., Pajevic, S., Jones, D.K., 2002. Virtual in vivo interactive dissection of white matter fasciculi in the human brain. *NeuroImage* 17, 77–94.
- Curran, K.M., Alexander, D.C., 2003. Orientation matching for registration of diffusion tensor images. In: *Proceedings of the SPIE Medical Imaging*.
- Curran, K.M., Alexander, D.C., 2004. Orientation coherence optimisation in tensor image registration. In: *Proceedings of the MIUA*.
- Fletcher, P.T., Joshi, S.C., 2004. Principal geodesic analysis on symmetric spaces: statistics of diffusion tensors. In: *Proceedings of the CVAMIA and MMBIA Workshops*.
- Friston, K.J., Ashburner, J., Frith, C.D., et al., 1995. Spatial registration and normalization of images. *Human Brain Mapp.* 2, 165–189.
- Friston, K.J., Holmes, A.P., 1995. Statistical parametric maps in functional imaging: a general linear approach. *Human Brain Mapp.* 2, 189–210.
- Gallier, J., 2000. *Geometric Methods and Applications, for Computer Science and Engineering*. Texts in Applied Mathematics. Springer Verlag, New York.
- Gee, J.C., Alexander, D.C., 2005. Diffusion-tensor image registration. In: Welckert, J., Hagen, H. (Eds.), *Visualization and Image Processing of Tensor Fields*. Springer, Berlin.
- Gerig, G., Gouttard, S., Corouge, I., 2004. Analysis of brain white matter via fiber tract modeling. In: *Proceedings of the IEEE EMBS*, pp. 4421–4424.
- Guimond, A., Guttman, C.R.G., Warfield, S.K., Westin, C.F., 2002. Deformable registration of DT-MRI data based on transformation invariant tensor characteristics. In: *Proceedings of the ISBI*.
- Hellier, P., Barillot, C., Memin, E., Perez, P., 2001. Hierarchical estimation of a dense deformation field for 3-d robust registration. *IEEE Trans. Med. Imag.* 20 (5), 388–402.
- Jones, D.K., Griffin, L.D., Alexander, D.C., Catani, M., Horsfield, M.A., Howard, R., Williams, S.C.R., 2002. Spatial normalization

- and averaging of diffusion tensor MRI data sets. *NeuroImage* 17, 592–617.
- Jones, D.K., Simmons, A., Williams, S.C.R., Horsfield, M.A., 1999. Non-invasive assessment of axonal fibre connectivity in the human brain via diffusion tensor MRI. *Magn. Reson. Med.* 42, 37–41.
- Kubicki, M., Westin, C.-F., Maier, S.E., et al., 2002. Diffusion tensor imaging and its application to neuropsychiatric disorders. *Harvard Rev. Psychiatry* 10, 324–336.
- Lester, H., Arridge, S.R., 1999. A survey of hierarchical non-linear medical image registration. *Pattern Recognit.* 32, 129–149.
- Little, J.A., Hill, D.L.G., Hawkes, D.J., 1997. Deformations incorporating rigid structures. *Comput. Vis. Image Understand.* 66, 223–232.
- Maintz, J.B.A., Viergever, M.A., 1998. A survey of medical image registration. *Medical Image Anal.* 2, 1–36.
- Mori, S., Crain, B.J., Chacko, V.P., van Zijl, P.C.M., 1999. Three dimensional tracking of axonal projections in the brain by magnetic resonance imaging. *Ann. Neurol.* 45, 265–269.
- Mori, S., Kaufmann, W.E., Davatzikos, C., et al., 2002. Imaging cortical association tracts in the human brain using diffusion-tensor-based axonal tracking. *Magn. Reson. Med.* 47, 215–223.
- Mori, S., van Zijl, P.C.M., 2002. Fiber tracking: principles and strategies – a technical review. *NMR in Biomedicine* 15, 468–480.
- Pajevic, S., Pierpaoli, C., 1999. Color schemes to represent the orientation of anisotropic tissues from diffusion tensor data: application to white matter fiber tract mapping in the human brain. *Magn. Reson. Med.* 42, 526–540.
- Park, H.-J., Kubicki, M., Shenton, M.E., et al., 2003. Spatial normalization of diffusion tensor MRI using multiple channels. *NeuroImage* 20, 1995–2009.
- Park, H.-J., Westin, C.-F., Kubicki, M., et al., 2004. White matter hemisphere asymmetries in healthy subjects and in schizophrenia: a diffusion tensor MRI study. *NeuroImage* 23, 213–223.
- Pennec, X., Fillard, P., Ayache, N., 2004. A Riemannian framework for tensor computing. *Int. J. Computer Vision* 66, 41–66.
- Press, W.H., Flannery, B.P., Teukolsky, S.A., Vetterling, W.T., 1993. *Numerical Recipes in C: The Art of Scientific Computing*, second ed. Cambridge University Press, Cambridge.
- Ruiz-Alzola, J., Westin, C.F., Warfield, S.K., Alberola, C., Maier, S., Kikinis, R., 2002. Nonrigid registration of 3d tensor medical data. *Med. Image Anal.* 6, 143–161.
- Stieltjes, B., Kaufmann, W.E., van Zijl, P.C.M., et al., 2001. Diffusion tensor imaging and axonal tracking in the human brainstem. *NeuroImage* 14, 723–735.
- Studholme, C., Hill, D.L.G., Hawkes, D.J., 1998. A normalised entropy measure of 3d medical image alignment. In: *Proceedings of the SPIE Med Imaging*, pp. 132–143.
- Wakana, S., Jiang, H., Nagae-Poetscher, L.M., van Zijl, P.C., Mori, S., 2004. Fiber tract-based atlas of human white matter anatomy. *Radiology* 230 (1), 77–87.
- Xu, D., Mori, S., Shen, D., van Zijl, P.C.M., Davatzikos, C., 2003. Spatial normalization of diffusion tensor fields. *Magn. Reson. Med.*, 175–182.
- Xu, D., Mori, S., Solaiyappan, M., van Zijl, P.C.M., Davatzikos, C., 2002. A framework for callosal fiber distribution analysis. *NeuroImage* 17, 1131–1143.
- Xue, R., van Zijl, P.C.M., Crain, B.J., et al., 1999. In vivo three-dimensional reconstruction of rat brain axonal projections by diffusion tensor imaging. *Magn. Reson. Med.* 42, 1123–1127.
- Yushkevich, P.A., Piven, J., Cody, H., Ho, S., Gee, J.C., Gerig, G., 2006. User-guided level set segmentation of anatomical structures with ITK-SNAP. *NeuroImage* 31, 1116–1128.
- Zhang, H., Yushkevich, P.A., Gee, J.C., 2004. Registration of diffusion tensor images. In: *Proceedings of the Computer Vision and Pattern Recognition*.
- Zhang, H., Yushkevich, P.A., Gee, J.C., 2005. Deformable registration of diffusion tensor MR images with explicit orientation optimization. In: *Proceedings of the MICCAI*.